

Probing electrically driven nanojets by energy and mass analysis in vacuo

Luis Javier Perez-Lorenzo¹ and Juan Fernandez de la Mora^{1,†}

¹Department of Mechanical Engineering and Materials Science, Yale University, 9 Hillhouse Avenue, New Haven, CT 06511, USA

(Received 30 December 2020; revised 14 August 2021; accepted 27 August 2021)

Time of flight (TOF) and energy analysis in vacuum are used in series to determine jet velocity U_j , diameter d_j , electrical potential V_j and energy dissipated ΔV at the breakup point of electrified nanojets of the ionic liquid 1-Ethyl-3-methylimidazolium tris(pentafluoroethyl)trifluorophosphate (EMI-FAP) (Ignat'ev *et al.*, *J. Fluorine Chem.*, vol. 126, issue 8, 2008, pp.1150–1159). The full spray is periodically gated by a grid held at a high voltage V_g , and received at a collector where the measured flight times provide the distribution of drop speeds u . Varying V_g provides the bivariate distribution of drop energies ξ and velocities. The collector plate, centred with the beam axis, is divided into eight concentric rings, yielding the angular distribution of the spray current, and high resolution (u, ξ) values in the whole spray. The energies of various particles of given u are all well defined, but depend uniquely on u , even though u and ξ are in principle independent experimental variables. Slow and fast particles have energies respectively well above and below the capillary voltage V_e (1.64 kV). As previously shown by Gamero-Castaño & Hruby (*J. Fluid Mech.*, vol. 459, 2002, pp. 245–276), this behaviour is due to the 2-stage acceleration process, first jointly in the jet for all particles, and then separately for free flying drops or ions of different mass/charge. The measured two-dimensional distributions of u and ξ provide the jet velocity U_j ($\sim 0.44 \text{ km s}^{-1}$) and electrical potential V_j (1.2 kV) at the breakup point. All molecular ions originate near the breakup point rather than the meniscus neck. A measurable fraction of anomalously fast drops is observed that must come from Coulomb fissions of the main drops.

Key words: aerosols/atomization, electrohydrodynamic effects

1. Introduction

Electrified liquid cones of sufficiently conducting liquids can produce steady jets with diameters of 100 nm or less. This would offer a rare window into the field of nanofluid dynamics if it were possible to make theoretical predictions and probe experimentally such tiny objects. Various authors have modelled numerically the process of nanojet formation in Taylor cones (Higuera 2003; Collins *et al.* 2013; Gamero-Castaño & Magnani 2018, 2019). The measured relation between the injected flow rate Q , the particle diameter and

[†] Email address for correspondence: juan.delamora@yale.edu

the emitted current I has provided a widely used test for these calculations (Gañán-Calvo *et al.* 2018). Other experimental insights on electrified nanojets have been obtained by studying not only in air but also in a vacuum the drops produced following jet breakup (Krohn 1961; Gamero-Castaño & Hruby 2001) by time of flight mass spectrometry. This information, however, relates only indirectly to the original jet through the breakup dynamics, and is generally more complex than the process of steady jet formation. Only three approaches yielding jet information have been so far demonstrated. The first and most detailed was direct imaging of the meniscus tip in vacuo by electron microscopy (Gabovich 1983; Benassayag, Sudraud & Jouffrey 1985). The method has been demonstrated only for liquid metals, which are uniquely able to withstand bombardment by energetic electrons. This approach may perhaps be extensible to simple inorganic molten salts, but would be difficult to apply to the labile molecular substances forming the vast majority of electrolytes used in the study of Taylor cones. One notable approach applicable to molecular liquids has used energy and velocity measurements in vacuo from sprays involving two distinct particles (Gamero-Castaño & Hruby 2002; Gamero-Castaño 2008, 2010, 2019). From the two pairs of measured particle energies and velocities, the velocity and electrical potential of the jet at its breakup point may be inferred. These two quantities also determine the energy dissipated by viscosity and ohmic conduction, which plays an important role in the structure of electrified liquid cones (Gamero-Castaño 2010, 2019). In addition, the known liquid flow rate reveals the jet diameter. Another approach applicable to molecular liquids has exploited the fact that the high electric fields acting on the meniscus often activate the evaporation of ions from the regions of the interface where such fields are strongest. In the case of low viscosity liquids like formamide and propylene carbonate, most of this emission takes place at the transition between the cone and the jet. Measuring these ion currents provides information on the magnitude of this maximal field when the kinetics of ion evaporation are known (Gamero-Castaño & Fernández de la Mora 2000; Guerrero *et al.* 2007).

In the present article we follow the strategy developed by Gamero and colleagues to infer jet properties based on energy and velocity analysis, with several innovations. First, we use eight concentric collectors, which yields not only the angular distribution of the full spray, but also relatively high resolution in both energy and velocity. In addition, for each spray angle, we determine the full two-dimensional (bivariate) distribution $I(u, \xi)$ of drop velocities and energies by performing energy and velocity analysis in series, rather than separately determining in parallel two univariate energy $I(\xi)$ and velocity $I(u)$ distributions. This two-dimensional distribution is naturally slower to acquire, but facilitates the determination of jet properties in the case of complex sprays composed of many particle classes rather than made up predominantly of two charged species (main drops and satellites, drops and ions, etc.). Following our earlier report of this bivariate measurement (Perez-Lorenzo & Fernandez de la Mora 2019), Gamero-Castaño & Cisquella-Serra (2021) have presented a detailed study of several sprays for the centre of the beam, measuring not only the bivariate $I(u, \xi)$ distribution, but doing so with a considerably more refined (differential) definition of the energy distribution.

For brevity, the usual term ‘stopping voltage’ is denoted here ‘energy’, even though it is in reality an energy per unit charge and has units of Volt.

2. Experimental

2.1. Vacuum facility

The apparatus shown schematically in figure 1 is similar to prior time of flight (TOF) set-ups (Gamero-Castaño & Hruby 2002), with several variations to be noted. Briefly, the

Probing electrically driven nanojets

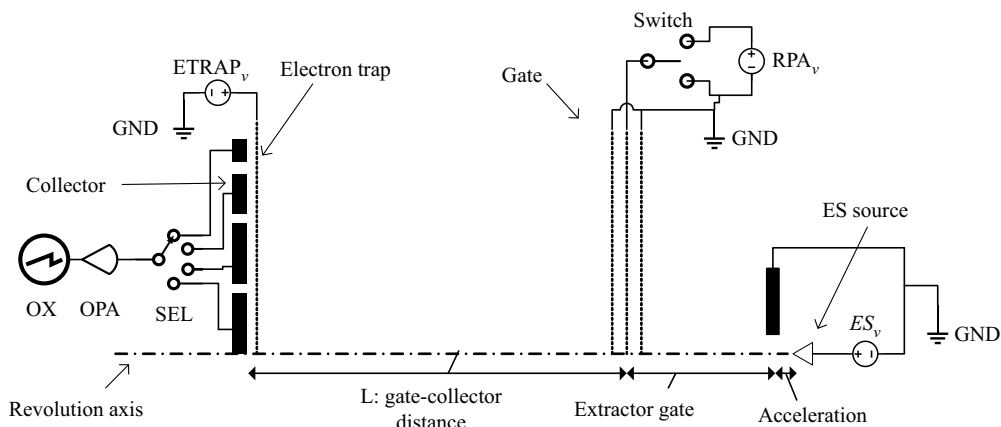


Figure 1. Sketch of the experimental apparatus with a segmented collector providing angular resolution. The gate is cycled between ground and a controllable voltage V_g , enabling the determination of the two-dimensional distribution of particle energies (related to V_g) and velocities (related to flight time from gate to collector). $L = 160.7$ mm; extractor-gate distance $L_{EG} = 35$ mm; emitter–extractor distance ~ 1.5 mm.

emitter capillary raised to a high voltage V_e faces a perforated extractor electrode held at ground at a distance ≈ 1.5 mm from the capillary tip, such that the spray particles pass through the perforation ($D = 3$ mm) into a field-free region. A short distance downstream, the charged particles encounter a gate made of two external grounded grids guarding a middle grid (the gate) that can be rapidly switched between a high voltage V_g and ground. When the gate is initially held at voltage V_g , charged particles with energies larger than V_g pass through it and reach the detector (left). A TOF curve $I(t)$ measures the current captured at the detector as a function of time t elapsed after the gate is suddenly grounded. This TOF curve then provides information of the arrival time for ions with energies below V_g . A series of N measurements with N different grid voltages V_g is undertaken with V_g varying from zero to ≈ 1.5 times the voltage V_e applied at the emitting capillary. This set of TOF curves then yields two-dimensional (2-D) information on the bivariate distribution of arrival time and energy of the spray particles $I(t, V_g)$. This 2-D distribution is considerably more informative than the separate measurement of the one-dimensional (1-D) energy and the 1-D TOF spectra, especially when drops with many different mass/charge ratios (m/q) are produced. An example of these TOF curves is given in figure 2 (cations of the ionic liquid 1-Ethyl-3-methylimidazolium tris(pentafluoroethyl)trifluorophosphate (EMI-FAP)) when all energies are included (highest V_g), although only the signal for the fastest particles is shown. When representing TOF curves for V_g values small enough for some energetic particles to go through the gate, the current measured at $t < 0$ (associated with particles having energies above V_g) is subtracted from the signal, so that all curves start at zero current. The two sharp steps shown in figure 2 correspond to ions, comprising approximately 30 % of the total spray current.

Because the particle beam expands spherically, the arrival time on a planar collector normal to the beam axis is given in terms of its spherical distance r to the gate: $t = r/u = L/(u \cos \theta)$, where L is the axial distance between the gate and the collector and θ is the polar angle relative to the beam axis. Therefore, $u = L/(t \cos \theta)$. Because θ may be as large as 20° – 30° , the resolving power in energy and velocity is severely limited in the common single planar collector configuration. One way to sidestep this problem is to use a spherical collector (Miller & Lozano 2020). In the present study the

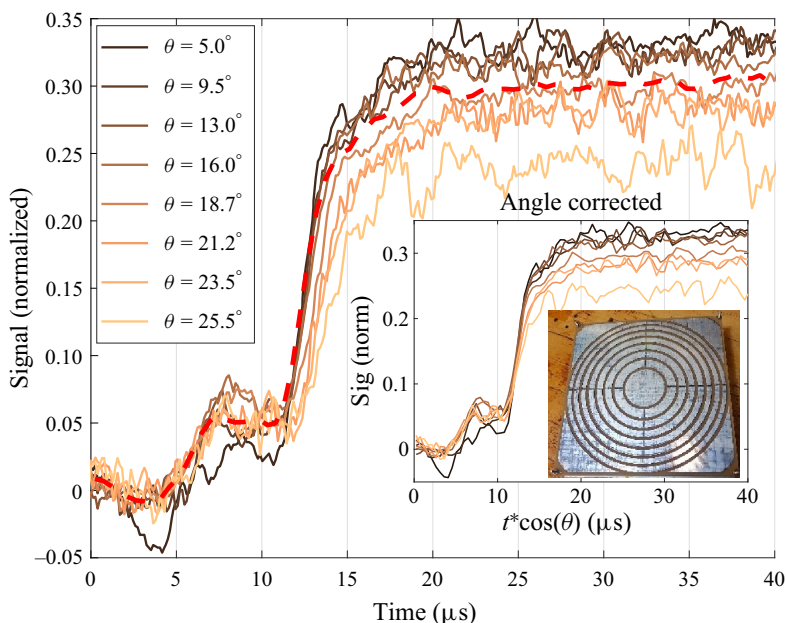


Figure 2. Arrival time curves (at maximum energy) focusing on the two fastest particles (two ionic steps on the left) for EMI-FAP in positive mode. The horizontal axis in the main figure, exhibiting horizontal shifts for the eight different collectors, is the uncorrected arrival time t . This shift is suppressed in the middle inset, where the horizontal axis is $t \cos \theta$. This inset also displays an image of the detector featuring its eight collectors. The dashed line represents the normalized angle-corrected sum of the signal of these eight collectors.

collector is composed of eight concentric rings (right inset to figure 2), providing angular beam information. Furthermore, the modest range of polar angles subtended by each collector increases drastically energy and velocity resolution. To verify that the axis of the spray matches closely the axis of the detector, prior to each experiment, we compare the currents received on the four corner regions of the collector. Under most conditions none of these corner regions receives any current, confirming that the full beam is within the collector's range. Centring is verified in separate calibration runs where the detector is moved closer to the emission source, so that a measurable current reaches the four corner detectors.

The effectiveness of the angular correction is seen in figure 2, where the various steps in the collected current curves start at the same time when plotted versus $\tau = t \cos \theta$ (inset), but not when plotted versus t (main figure). This correction may be viewed as a representation of the TOF curves versus the particle velocity based on the real flight distance $L / \cos \theta$. Similarly, the gate only affects the axial component of the kinetic energy of the particles, precluding their axial progress towards the collector based solely on the value $m(u \cos \theta)^2 / (2q)$. Accordingly, the voltage variable corresponding to each collector is divided by $\cos^2 \theta$ in order to represent the total (spherical) rather than the axial kinetic energy.

2.2. Liquid selection

A leading motivation for this work was to identify propellants suitable for electrospray propulsion *in vacuo*, with a special interest in ionic liquids (ILs) composed of particularly heavy anions and cations. Among the heaviest IL anions known is the FAP family

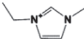
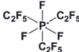
Density	Viscosity	Electrical conductivity	Surface tension	Cation EMI ⁺	Anion FAP ⁻
1.715 ^a (g cm ⁻³)	73.98 ^b (mPa s)	0.45 ^b (S m ⁻¹)	35.3 ^a (dyn cm ⁻¹)		

Table 1. Properties of EMI-FAP at 20 °C.

^aSoučková, Klomfar & Pátek (2012). ^bSeki *et al.* (2012).

Emitter voltage (V)	Average current (nA)	Flow rate (10 ⁻⁹ kg s ⁻¹)
-1642	-307	1.38

Table 2. Main features of the negative electrospray of EMI-FAP investigated here by TOF and retarding potential.

with the general formula $\text{PF}_3(\text{C}_n\text{F}_{2n+1})_3^-$, having been synthesized with n up to 4, and molecular mass $m = 754$ amu (Ignat'ev *et al.* 2005). We have previously studied electrosprays of tris(pentafluoroethyl)trifluorophosphate ($\text{PF}_3(\text{C}_2\text{F}_5)_3^-$) paired with the cation 1-Pentyl-3-methylimidazolium, which gave negative monomer and dimer ions with masses 445 and 1043 amu. However, its relatively high viscosity and modest electrical conductivity produced inadequately low spray currents of ~ 10 nA (Larriba *et al.* 2007). Here, we investigate the salt formed by the same anion paired with 1-Ethyl-3-methylimidazolium⁺ (EMI⁺), which is several times more conducting and less viscous (table 1) and emits currents between 200 and 1000 nA.

The sample used of EMI-FAP (Merck) was degassed by placing it under a modest vacuum (~ 100 mTorr) at 80 °C for approximately 24 h. After this step, only dry air was used to pressurize the sample container. The sample was electrosprayed out of a sharpened silica capillary, and its flow rate to the tip was controlled through the pressure applied to the liquid reservoir. The emission properties are collected in table 2. All of the experiments were carried out at a chamber pressure of approximately 4×10^{-6} Torr, with an axial distance $L = 160.7$ mm from the central mesh of the gate to the surface of the collector.

While EMI-FAP is the only liquid we have so far studied in this facility, we intend to exploit it with many other electrolytes and ILs. The instrument would nevertheless be limited in situations with small ion currents, since the signal is dispersed in three dimensions (angle, velocity and energy).

2.3. Spraying regime

The experiments reported were all in the steady cone-jet regime. We monitor the current and the meniscus shape continuously with a long focal length microscope of high resolving power. We can distinguish the various shapes of the meniscus and complement this visual information by comparing the measured current with the expected cone-jet value. Unsteady operation is easily identifiable as the emission tip becomes blurry and the emission current drops (actually the frequency of emission is small enough to measure it on the electrometer ~ 9 kHz). All the experiments reported have passed these identity tests.

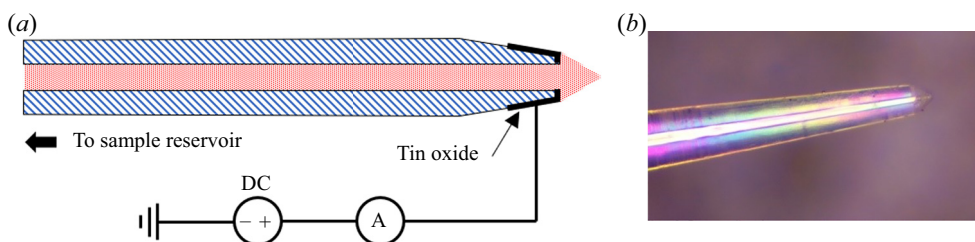


Figure 3. (a) Diagram of the silica capillary emitter, with a ~ 5 mm long section made conductive by chemical vapor deposition of SnO_2 (rainbow colour pattern on the right image). A thin PtIr alloy cable (b) provides the high voltage to the SnO_2 coating, which touches and electrifies the liquid meniscus.

2.4. Application of the high voltage to the meniscus

In preliminary experiments we applied a high voltage V_{vial} to the liquid reservoir and inferred the voltage at the tip of the non-conducting capillary as $V_e = V_{\text{vial}} - IR$, where I is the measured electro spray current and R is the resistance of the liquid inside the capillary, calculated based on the known liquid conductivity and the geometry of the capillary. In order to determine the power irreversibly dissipated during jet acceleration it is important to have a direct measurement of V_e . Therefore, for the experiments reported here we coat the capillary tip with a semiconducting tin oxide film to which we directly apply the high voltage V_e . The film is deposited by evaporating tin(II) chloride in a flow of oxygen within a heated quartz tube. At the exit of this tube, tin oxide vapours condense on a previously sharpened silica capillary whose tip region is kept within the hot tube. The commercial capillary (Polymicro Technologies; 50 μm inner diameter (ID), 360 μm outer diameter (OD)) is externally coated with a layer of polyimide, except for its last few mm where the polyimide coating is burnt. Prior to depositing the oxide film, the glass is pulled under a torch into a tip ID of approximately 25 μm , the outer wall is sharpened mechanically to an outer OD of some 50 μm . This end region is fragile, so the electrical contact is made through a 50 μm spring-shaped thin platinum–iridium wire 80 : 20 alloy. The resistivity of the coating across its length is in the range of 1–100 $\text{k}\Omega$, while that of the PtIr cable was calculated to be approximately 50 $\text{k}\Omega$. The coated length is limited by partially covering the capillary with a glass sleeve during the deposition process, so that only a few mm of the tip are conductive (figure 3).

Only a few positive polarity experiments were successfully conducted with the current set-up. Apparently, the electrolytic reactions between the deposited SnO_2 and the IL dissolves the conductive coating of the capillary within the span of an hour. Previous experiments using a thin PtIr wire inside the capillary to electrify the meniscus were successful in both polarities. Electrochemical reactions may change substantially the composition of the liquid when the emissions have the high charge/mass ratios typical of purely ionic emissions (Lozano & Martinez-Sanchez 2004), but not so in the drop emission regime studied here.

To determine the volumetric rate of liquid Q from the reservoir to the meniscus, its relation $Q(\Delta p)$ to the pressure drop Δp across the tube was calibrated. Under usual emission conditions, a small air bubble was introduced at the inlet of the capillary. The bubble motion was tracked across a calibrated length so that, for a given condition (backpressure, tip voltage), the flow rate, defined as capillary cross-section times measured drop velocity, could be inferred with an estimated error of approximately 2% (mostly due to the ambiguity of the capillary ID = 50.6 ± 0.4 μm). Several measurements were performed spanning the expected experimental parameter space. The bubble-based flow

Probing electrically driven nanojets

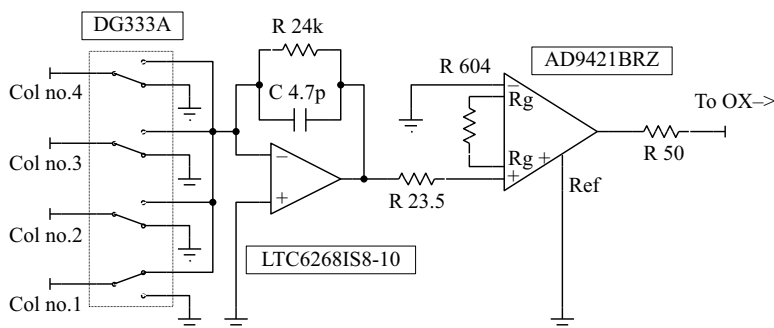


Figure 4. Simplified diagram of the electrometer, featuring the collector selector (Vishay DG333A, showing Col no.1 active, the rest are grounded), current-to-voltage conversion and post-amplification for a single electrometer channel. The operational amplifier (Linear Technology LTC6268IS8-10) acts as virtual ground for the selected collector, converts current to voltage with a gain of -2.4×10^4 V/A from DC to 1.4 MHz (-3 dB point) while the instrumentation amplifier (Analog Devices AD8421BRZ) in the current configuration has a gain of 17.39 V/V from DC to ~ 2 –10 MHz (-3 dB point). The output of the amplifier is wired to the output signal connector through a 50Ω resistor (0.5 V/V amplification when used with a 50Ω termination on the other end). Col, collector.

rates were found to be similar to those determined from Poiseuille's relation $\Delta p = 8\mu LQ/\pi R^4$, where R is the inner radius of the tube. Subsequently, flow rates were determined using Poiseuille's law taking into account the temperature-dependent viscosity for each experiment. Due to the steep temperature dependence of the viscosity, these measurements may have up to $\pm 4.4\%$ error at just 22 ± 1 °C. Despite these precautions, the disagreement between the liquid flow rate determined from the pressure drop and that inferred from the velocity and energy distributions was substantial ($\sim 40\%$), even after correcting Q for the difference between emitted and collected current. A possible explanation for the discrepancy is that the capillary was partially clogged after calibration.

2.5. Detector

A fast electrometer was developed for this experiment. Good noise isolation is achieved by placing the amplification electronics inside the vacuum chamber directly behind the collector, thus avoiding long cables that increase the collector capacitance and the likelihood of electrical noise. As shown in figure 4, the collector features several insulated regions that can be electrically connected to either a current-to-voltage converter or ground. The electrical connections are controlled externally via the acquisition software that cycles through them to acquire data from each of the individual collectors. In order to increase the acquisition speed, the electrometer is divided into three physical channels, each with its own current-to-voltage converter and collector selector so that a 4-channel oscilloscope (Keysight DSOX2004A) could acquire three signals at once, dividing the overall acquisition time by 3 (the fourth oscilloscope channel was reserved for synchronization).

2.6. Collector

The charged particles are received in a flat printed circuit board that features several insulated current-collecting regions placed perpendicularly to the axis of the emitter (inset to figure 2). The current-collecting regions are located between a ground plane and an electron trap (figures 1 and 5) held at a constant voltage (-9.6 V) to repel

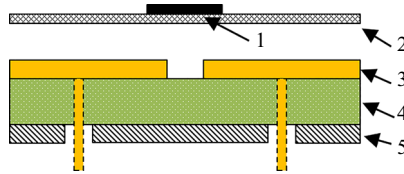


Figure 5. Collector plate cross-section diagram: mask (1), secondary electron suppressor mesh (2), current-collecting regions (3) with vertical buried electrical contact (dashed), insulator (4) and ground plane (5). The electronics is placed in a separate board below the ground. The mask is a thin stainless steel sheet covering the insulating regions, intended to avoid deposition of IL over the insulating gaps.

secondary electrons released by impact of the ions on the collector plate. This electron trap is formed by several masks spot welded to a stainless steel wire mesh that is 88.36 % transparent. The gap between the collectors and the electron trap mesh was set to ~ 6 mm. Note that the combined active region of the collector plate is severely limited by the mask-shadowed regions, (mask transparency ~ 70 %) and by the overall transparency of the four steel meshes required for beam control (~ 60 %). Overall, the electrometer only collects approximately 42 % of the beam current.

2.7. Gate

The gate is formed by three stainless steel meshes (TWP Inc. 050X050T0012W48, 50×50 wires per 2.54 cm, wire diameter of $30 \mu\text{m}$, transparency 88.36 %) welded to electrically conducting support frames that keep them under tension. The three meshes are positioned 3.7 mm apart from each other using nylon insulators. The central support frame is connected to a high voltage pulser (Behlke, HTS 201-03-GSM option S-TT) wired so that the output is tied to either a high voltage power supply or ground. The fall time of this high voltage square waveform is about 300 ns. All the experiments were carried out starting from a steady state high voltage at the gate (V_g), transitioning to ground at $t = 0$.

2.8. Data processing

The signals (Volts) detected by the amplifier are recorded on a computer as tables of $V(t, V_g, j)$, where j represents a specific collector, therefore a flight angle θ_j . Each experiment includes a blank run where the electrospray source is off. These blank experiments are used to subtract repeatable electrical noise from the received signal. Previous to this subtraction, a moving average per channel is applied to the signal and blank data, using 30 points in time for a $\sim 2 \mu\text{s}$ window, and 3 points in energy for a ~ 124 V window (2 points only on the edges). The subtracted signal is shifted vertically by the mean signal level before the trigger event ($t < 0$), therefore setting this as zero. The region 0 – $2 \mu\text{s}$ is also set to this level. The noise-corrected zeroed voltage signal is converted into a received current signal through the known amplifier gain (figure 4), and into a corrected current signal by applying the transparency factor from table 3 (see section A in the supplementary material available at <https://doi.org/10.1017/jfm.2021.771>). This is what we define as the corrected signal. All the data presented in this work are given based on this correction unless otherwise noted, with the exception of the propulsive parameters. The propulsive parameters whose values are directly proportional to the current (mass flow rate \dot{m} , and thrust T) are, to a first approximation, initially computed based on corrected current data. Nevertheless, in view of the discrepancy between the emission current directly measured and the total current received computed from the sum of corrected currents, they have been additionally rescaled by the ratio of these two currents. From table 2 and the largest received cumulative corrected current from figure 6(a), this scaling factor is 1.21

Collector #	1	2	3	4	5	6	7	8	9–12 ^c
r_1^a (mm)	0	25.6	38.4	49.2	59	68.3	77.2	85.6	93.4 ^c
r_2^a (mm)	22.6	35.4	46.2	56.1	65.4	74.2	82.6	90.5	102.9 ^c
Transparency ^b	0.609	0.608	0.606	0.604	0.602	0.600	0.597	0.595	0.591

Table 3. Geometrical characteristics of the regions of the collector plate; $L=0.1607$ m.

^aInner and outer radii of the masks on the electron trap. The actual size of the physical current collector is slightly larger, having regions shadowed by the mask.

^bFour meshes 88.4% transparent, corrected for beam inclination.

^cCorner collectors (second inset in figure 2).

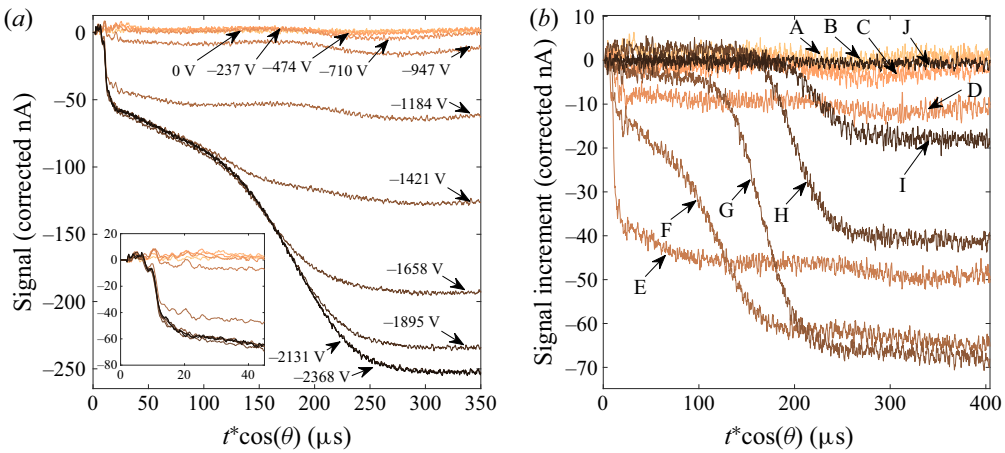


Figure 6. Selection of time of flight curves $I(t, V_g)$ for a subset of stopping potentials $\xi_g = V_g/\cos^2\theta$ (Volt) = $-\{0, 237, 474, 710, 947, 1184, 1421, 1658, 1895, 2131, 2368\}$ (light to dark). The left figure shows raw cumulative $I(t \cos\theta, \xi_g)$ spectra from which the current measured at $t < 0$ is subtracted from the signal. The inset shows a detail of the fastest particles. The differential curves on the right (light to dark) are the differences between consecutive pairs of curves on the left: A, $I(t \cos\theta, -237 \text{ V}) - I(t \cos\theta, 0 \text{ V})$; B, $I(t \cos\theta, -474 \text{ V}) - I(t \cos\theta, -237 \text{ V})$, etc. This figure was generated by combining the curves from all collectors as described in § 2.8.

for the room temperature experiment. The time variable is shortened in all cases by 430 ns to account for the gate switch internal delay (150 ns), the gate fall time (0.5×300 ns) and the electrometer rise time (≈ 130 ns). The tables of corrected signal $I(t, V_g, j)$ are converted into $I(\tau, \xi_g, j)$ via

$$\tau = t \cos\theta, \quad \xi_g = V_g/\cos^2\theta. \quad (2.1a,b)$$

The conversion $\xi_g = V_g/\cos^2\theta$ follows from the fact that the gate meshes are flat and perpendicular to the axis of emission, and will reject particles according to their axial velocity.

Data are then binned into a common set of ≈ 1500 τ values, maintaining a time resolution of ~ 0.27 μs . For each collector j the current signal between two contiguous ξ_g is subtracted creating the current increment for a given energy increment: $\Delta I_n(\tau, \xi, j) = I(\tau, \xi_{g_n}, j) - I(\tau, \xi_{g_{n-1}}, j)$, where ξ is defined as the intermediate energy $(\xi_{g_n} + \xi_{g_{n-1}})/2 = \xi$. The signal increments ΔI are ordered among all collectors by increasing energy values to obtain $\Delta I(\tau, \xi_i)$. Reconstructed cumulative signals are generated as $I(\tau, \xi_k) = \sum_{i=1}^k \Delta I(\tau, \xi_i)$ for the joint set of all collectors (angular information is lost).

The error associated with this energy assignment is $\approx(\xi_{g_n} - \xi_{g_{n-1}})/2$, which for the conditions of the experiments shown here (40 linearly spaced V_g values) is ± 26 V for the innermost and ± 32 V for the outermost collector. The error associated with the variation in $\cos^2(\theta)$ within a given collector is at most 1.1 % (worst case for collector no.8). Note that the moving average smears fast changes in time and velocity but does not reduce the number of data points except near the boundaries (where the number of data averaged is less than elsewhere).

3. Results

Figure 6(a) represents the TOF signal obtained at various ξ settings. Figure 6(b) is obtained from the difference between pairs of curves in figure 6(a), taken at consecutive energies. The curves in figure 6(b) therefore correspond to the TOF spectrum for particles having energies in the interval between those for the two curves subtracted. In spite of the few ξ values used, there is a well-defined step in each of these energy-resolved TOF curves, indicating that particles contained within a narrow energy range have a relatively narrow range of velocities. Figure 6(b) shows also that the fastest particles have the smallest energies.

The full 2-D dependence of the corrected charged particle current versus the two corrected energy and velocity variables is represented as a contour map in figure 7. Panel (a) shows the data in their original cumulative form $I(\tau, \xi)$, where the current rises monotonically with both independent variables. Note that the boundaries of the various contours (fixed current) approximate the ‘corner’ shape of a right angle. If these contours were perfect corners all cumulative distributions would be step functions and their differential forms would give delta distributions. Figure 7(b) is the contour map version of the corresponding differential representation $\partial^2 I(\tau, \xi)/\partial\tau\partial\xi$, which converts the succession of sharp corners at each energy in (a) into peaks in (b), collectively producing a ridge-like feature. While figure 6 involves just a set of 11 ξ_g values from the data pool, figure 7 has been generated using the full experimental range comprising 313 different ξ values (40 fixed gate voltages, at 8 angles excluding the repeated $V_g = 0$). Here, $\partial^2 I(\tau, \xi)/\partial\tau\partial\xi$ is inferred from the cumulative distribution in (a) by fitting it to either a sine cosine sum (energy) or a spline (time), differentiated and then fitted to a single Gaussian in the energy space (top to bottom) or to three Gaussians in the time domain (left to right). Both the corners of the cumulative distributions or the peaks in the differential representation (top left to bottom right diagonal) reveal that, although charged particles have a wide range of velocities and energies, within a selected modest range of energies only a relatively narrow range of velocities is encountered. In other words, there is a close connection between particle velocity and energy.

The conclusions drawn from the 2-D representation of figure 7 may be similarly obtained from the differential representation on figure 6, except for the very low intensity lobe on the top right corner of figure 7. We shall argue that this lobe is an artefact resulting from charged particles contained within the gate electrodes while the gate voltage is transitioning.

4. Discussion

4.1. The origin of the relation between particle velocity and energy

An important feature of the data presented in figures 6 and 7(b) is that, while the emitter voltage is -1643 V, the fastest particles (the ions) include stopping potentials in the range from -1050 to -1200 V (mid-left boundary in figure 7b), and the slowest particles include

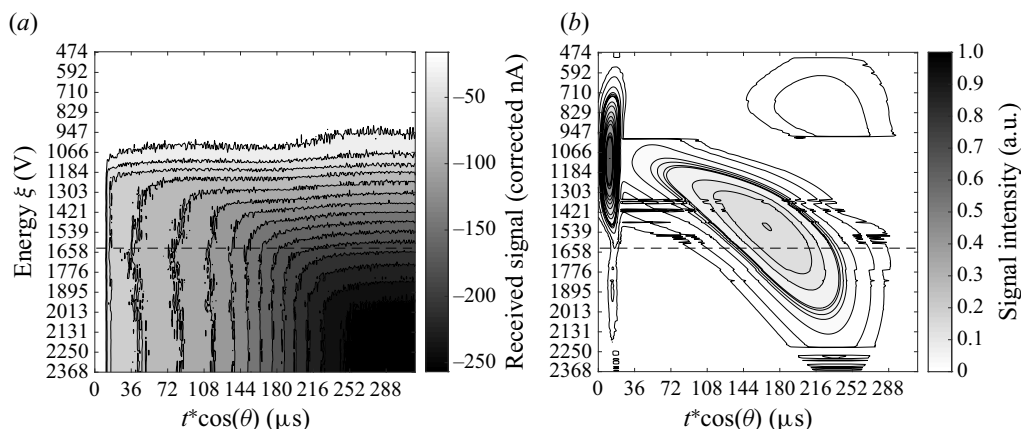


Figure 7. Intensity map showing the collected current as a function of the angle-corrected TOF and energy variables for the room temperature experiment (no features were found from 0 to -474 V or after $300 \mu\text{s}$ so the data displayed here exclude that empty range). The dashed line marks the emitter potential. (a) Original data in cumulative form in both axes. (b) Data in differential form in both axes, levels have been manually chosen to enhance the small signal features. Note that to obtain this representation substantial data manipulation is required, hence the presence of artefacts like the vertical line at $t \sim 18 \mu\text{s}$ or the horizontal cuts in the contour lines.

energies of some $2000 + \text{V}$ (mid-low boundary in figure 7b). Particles with well-defined velocities are therefore present in the beam with well-defined energies considerably larger as well as considerably smaller than the emitter voltage. This feature is independently demonstrated in figure 8, a close-up to the time of flight curves of the fastest particles for one negative spectrum. The various steps corresponding to monomers (FAP^-), dimers $[\text{EMI}^+(\text{FAP}^-)_2]^-$, trimers $[\text{EMI}^+_2(\text{FAP}^-)_3]^-$, ..., are all well resolved, demonstrating that all these ions have narrowly defined velocities. The red dashed line is the calculated TOF curve corresponding to an emission potential of -1200 V (estimated in table 7, row b, in § 4.8). Yet, the capillary tip was held at -1643 V . Although ion energies show the most extreme deviation from the emission voltage, most particles have anomalous energies, with a systematic and rather strong dependence of the energy on the velocity of each group of particles (figure 7b).

A way to understand why faster and slower particles have energies below and above V_e is to assume that a substantial fraction of the emitter voltage V_e is converted into kinetic energy of the jet prior to its breakup into drops (Gamero-Castaño & Hruby 2002; Gamero-Castaño 2008, 2010, 2019). This process is of course natural, since the kinetic energy evidently possessed by the jet must necessarily have an electrical origin. Let us accordingly assume that an electrified jet carrying a volumetric flow Q (mass flow rate ρQ , where ρ is the density of the ionic liquid given in table 2) and a current I accelerates from zero velocity at the capillary to a certain velocity U_j at the jet breakup point, at the expense of a certain voltage drop $V_e - V_j$, such that strict energy conservation would yield $\frac{1}{2}\rho QU_j^2 = I(V_e - V_j)$. In this expression we have neglected the surface energy term $2\pi\gamma R_j U_j$, where γ is the surface tension. This term is comparable to the kinetic energy term at the neck of the jet, but soon becomes negligible as the jet thins. A diversity of prior studies (Gamero-Castaño & Hruby 2002; Gamero-Castaño 2019) have argued that the process of jet acceleration is not completely reversible, but rather involves some viscous and ohmic dissipation, associated with a certain irreversible voltage drop ΔV . The voltage

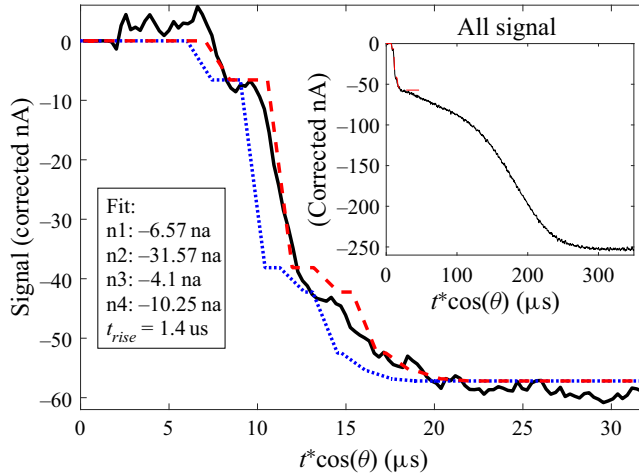


Figure 8. TOF curves at high energy for the fastest EMI-FAP cations at 20 °C (monomer, dimer and trimer ions), all exhibiting well-defined velocities (solid black line). Dotted and dashed lines are expected responses, at energies -1643 V (the emitter voltage V_e) and -1200 V, showing that the ions have energies well below V_e . The inset is the full spectrum, including the drops.

available to accelerate the jet is accordingly not V_e , but the slightly smaller quantity

$$V_o = V_e - \Delta V, \tag{4.1a}$$

$$\frac{\rho Q U_j^2}{2} = I(V_o - V_j). \tag{4.1b}$$

This process of conversion of electrical into kinetic energy of the bulk liquid continues until the point where the jet breaks up into drops, where (4.1b) will now be applied. Once the jet breaks up, each fragment released with a given mass m and charge q accelerates independently of the other drops down to the ground potential, increasing its kinetic energy by qV_j . Energy conservation then results in a total energy per unit charge

$$\frac{mu^2}{2q} = \xi = \frac{mU_j^2}{2q} + V_j. \tag{4.2a}$$

For each particle class we measure both, the energy ξ and the velocity u , in terms of which $m/q = 2\xi/u^2$. Equation (4.2a) may therefore be rewritten as the following relation between measurable quantities:

$$\xi = \xi \frac{U_j^2}{u^2} + V_j, \quad \text{or} \quad \frac{1}{\xi} = \frac{1}{V_j} \left(1 - \frac{U_j^2}{u^2} \right). \tag{4.2b,c}$$

Because for each spray both U_j and V_j are approximately fixed quantities, (4.2c) establishes a unique relation between the energy and the velocity of each particle class in that spray. In this scenario, plotting the measured inverse of the energy versus the measured inverse of the squared particle speed should give a straight line. If this were so, the intercept of this line with the vertical axis would give $1/V_j$, and its slope would be $-U_j^2/V_j$. This would provide an experimental method to determine these two important characteristics of the jet. Furthermore, a measurement of the flow rate Q combined with (4.1) would

give the irreversible voltage drop ΔV , while mass conservation $Q = U_j \pi R_j^2$ would give the jet radius R_j at the breakup point. In other words, combined energy and velocity measurements would provide a means to determine key characteristics of the jet at its breakup point that appeared to be unmeasurable prior to the studies of Gamero-Castaño & Hruby (2002).

The reason for the existence of particles with energies well above and below V_o becomes more transparent if we introduce the mean mass over charge

$$\frac{m_j}{q_j} = \frac{\rho Q}{I}, \quad (4.3)$$

use it to rewrite U_j in (4.1b) as

$$\frac{U_j^2}{2} = \frac{q_j}{m_j} (V_o - V_j), \quad (4.4)$$

and rewrite (4.2a) as (4.6) in terms of the dimensionless mass over charge α (4.5):

$$\alpha = \frac{m}{q} \frac{q_j}{m_j}, \quad (4.5)$$

$$\xi = \alpha V_o + V_j(1 - \alpha) = V_j + \alpha(V_o - V_j). \quad (4.6)$$

Particles with very small $m/q(\alpha \ll 1)$ would then have an energy close to V_j . As a reference, for the jet studied here having $m_j/q_j = 0.00445 \text{ kg C}^{-1}$, the dominant negative dimer ion ($m/z = 1001$ Dalton) has $\alpha = 0.00233$, so its energy should give the jet potential with little error. Particles with the mean m/q have $\alpha = 1$ and possess the mean energy V_o . Finally, particles with m/q larger than the average ($\alpha > 1$) may have energies well above V_o , as observed. There is an additional mechanism to be later discussed to produce particles with energies above V_o . Large highly charged drops originally released with energies comparable to V_o may subsequently lose some charge via ion evaporation or Coulomb explosions, therefore requiring a larger repulsive voltage to be stopped. However, this possibility would require that the charge be lost after the acceleration is substantially completed, while charge loss events in our work take place almost at the point of jet breakup.

4.2. Experimental determination of the jet properties at its breakup point

As a first approximation to the problem, we examine our data in figure 9 at relatively high energy resolution and with full angular information. Figure 9(a) shows the experimental cumulative curves $I(\xi_j, \tau)$ for collector 1 at 40 different energies ξ_j . When generating the 39 differential traces $\Delta I(\xi, \tau) = I(\xi_{j+1}, \tau) - I(\xi_j, \tau)$ obtained by subtracting consecutive curves from (a), the resulting noise is excessive. But upon applying a 10 μs moving average, their structure is more clearly shown as the smoother lines depicted in figure 9(b,c). This averaging naturally degrades the high frequency information in the original spectra. This degradation affects primarily the fastest particles (the ions), which will be analysed separately. The domain at $\tau > 40 \mu\text{s}$ relevant to the drops is undistorted by this averaging. For the remaining particles one confirms the structure seen in figure 6 involving primarily two steps, one for ions and another for considerably larger particles to be referred to as ‘drops’. The mean position of the fairly narrow ionic steps ($\tau \sim 10 \mu\text{s}$) is relatively independent of the energy. The drop steps are generally wider, with a mean position strongly dependent on the energy. In addition to these two dominant

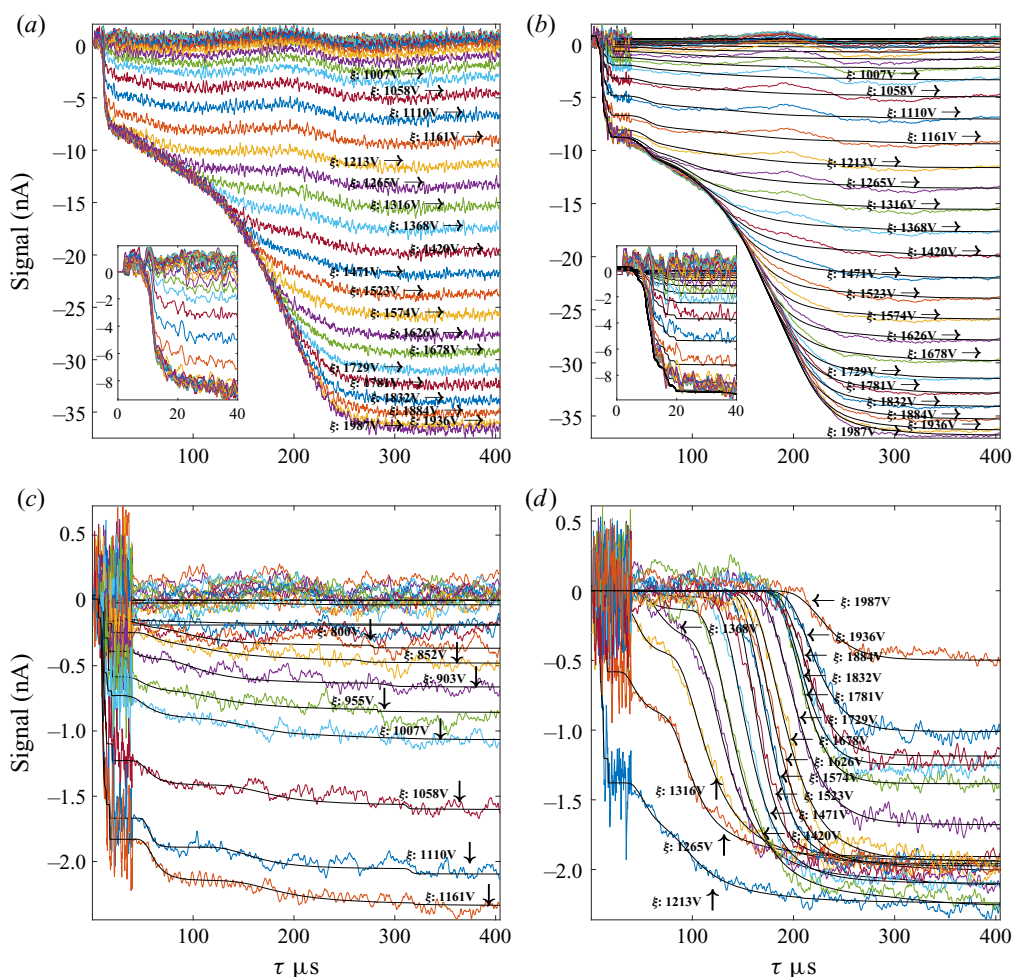


Figure 9. Spectra obtained for collector no.1 showing the following. Panel (a): the 40 experimental raw cumulative curves $I(\tau, \xi)$ for each of the gate potentials ξ_g . Panels (c) and (d): the 39 differential curves $\Delta I(\tau, \xi) = I(\tau, \xi_{j+1}) - I(\tau, \xi_j)$ obtained after applying a $10 \mu\text{s}$ moving average for $\tau > 40 \mu\text{s}$ (jagged lines) with their corresponding energy ξ , compared with their best fits (smooth black lines) to a sum of error functions of the velocity variable ($\sim 1/\tau$). Panel (b) contains the experimental cumulative spectra (wavy lines) with a $10 \mu\text{s}$ moving average for $\tau > 40 \mu\text{s}$, and the reconstructed cumulative fit (smooth black lines) obtained by adding the fits of the differential curves from (c) and (d).

steps clearly observable in figure 9, we shall be able to resolve unambiguously several other subtle features when averaging over all collectors (figure 10). For instance, the ion group includes separate steps for monomers dimer and trimers of EMI-FAP at a stopping potential $\sim 1100 \text{ V}$. Larger clusters are also present (tetramer, ...), but they cannot be individually resolved and will be accounted for as a single ‘cluster step’, broader than those for the monomer–trimer. Ion species will be addressed in a specific discussion below. The drop steps centred at $\tau > 150 \mu\text{s}$ are generally well defined by a single feature, although some curves include a small secondary step at relatively large τ , to be later discussed. The steps centred before $150 \mu\text{s}$ are more complex, including at least an additional lower step of faster particles, and in some cases two such smaller steps. Notice finally the presence of a small step of large drops (large τ) rising in some cases above the well-defined drop step.

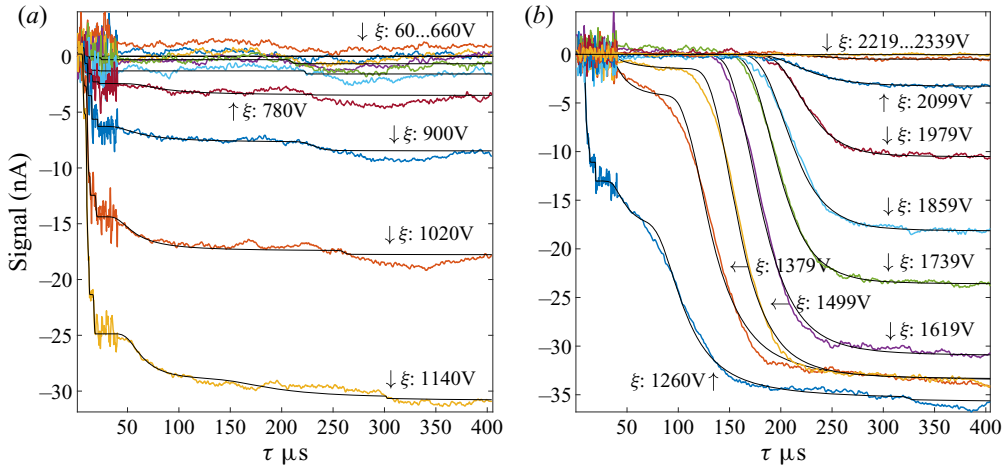


Figure 10. Result of binning $\Delta I(\xi, \tau, \theta)$ from the eight collectors (with full loss of angular information) into a set of equally spaced energy bins (midpoint values specified by the arrows). The $10 \mu\text{s}$ moving average is applied only for $\tau \geq 40 \mu\text{s}$. Curves at energies ξ of 1619, 1739 and 1859 V have been displaced vertically by +2, -1.5 and -0.5 nA, respectively, to correct for a displacement (of likely electrical origin) on the flat 0–100 μs region. Curves with final signal ≤ 0 were fitted as zero signal. The jagged lines are experimental data, while the smooth lines are error functions fits (4.7).

In order to capture more clearly these various smaller features and simplify the analysis, we have combined the curves among all angles and reduced the number of energies. To do so we select 21 equally spaced energies, and add up all of the $\Delta I(\xi, \tau, \theta)$ data whose energy is within two such consecutive energy bounds. This yields 20 energy-selected TOF curves $\Delta I(\xi, \tau)$ shown in figure 10. The energy of each curve is chosen as the midpoint between the bounds. For clarity the figure is divided into two panels corresponding to low (a) and high (b) energies. The same analysis is implemented in section C of the supplementary material, individually to each of the collectors and energies, resulting in 313 curves, evidently with a lower signal to noise ratio.

In view of the stepped structure of the experimental data in figure 10, we have fitted them using a linear combination of rising error functions of the form

$$I(u) = a_0 + \sum \frac{b_i}{2} \operatorname{erf} \left(\frac{u^n - c_i^n}{\sqrt{2}d_i} \right), \quad (4.7)$$

where c_i is the velocity at the step centre, while b_i and d_i measure the height and the width of each step. The values of n chosen to optimize the fit were $n = 1$ for ions, $n = 2$ for all drops.

Figure 9(b) shows the reconstructed cumulative curves obtained by adding the fits to the differential distributions in panels (c) and (d), and comparing them with a $13 \mu\text{s}$ running average of the original cumulative distributions. The comparison is fair, except that the fit does not have the slightly ascending regions (150–250 μs , where the signal goes up while it should go monotonically towards lower currents) present in some of the original data (averaged or not). These retrograde regions are unexpected, and cannot be represented by a combination of error functions with positive coefficients b_i and c_i (4.7). Comparison of the jagged and the smooth curves in panel (b) then shows that the fitting process may introduce erroneous features 1–2 nA in height in the cumulative curves (0.1 nA in the differential curves). These possible experimental errors are most prominent at the lowest energies.

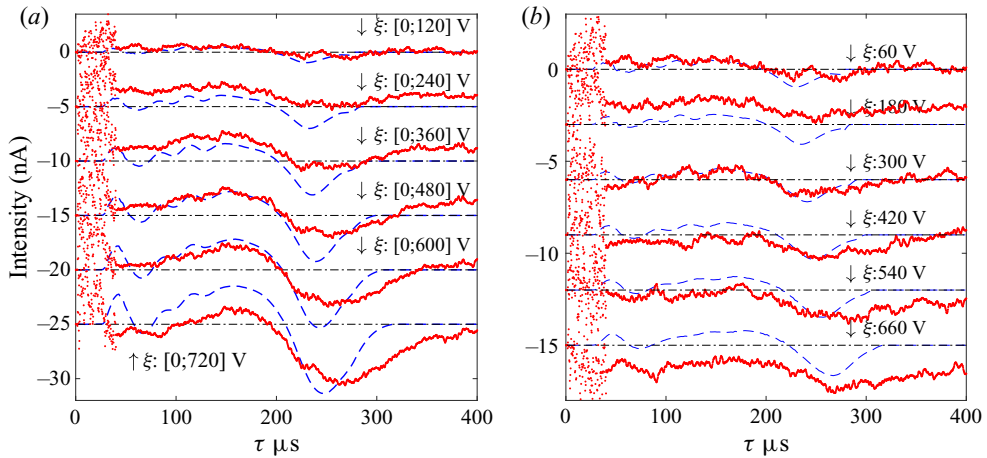


Figure 11. Retrograde regions within an energy range where no beam particles are expected (ξ : 0–720 V). (a) Cumulative signal $I(\xi, \tau)$. (b) Differential form $\Delta I(\xi, \tau)$ between consecutive energies. For clarity, consecutive plots are shifted vertically by 5 nA and 3 nA in (a) and (b), respectively. The dotted and dashed lines show, respectively, the data and the model calculations the supplementary material, section D, accounting for energy loss of ions within the gate at the instant of gating. The horizontal dash-dot lines are the zero level of each trace.

4.3. Retrograde regions

A lot of effort has been put into understanding the presence of a mysterious slow droplet step appearing within the 300–1400 V energy range (figure 11). In the cumulative representation this step is preceded and followed by a monotonically decreasing signal. When using the differential representation $\Delta I(\xi, \tau)$, a faint but repeatable step at $\tau \sim 200\text{--}300 \mu\text{s}$ appears, although its clarity is disturbed by the presence of the main droplet step at energies above 1000 V. These weak features are no longer observable at the highest energies in either the cumulative or the differential representations. For our TOF experiments, the received signal is expected to grow monotonically over time. Thus, the presence of regions where the signal decreases is anomalous. We believe these features are caused by energy loss on particles located between the gate electrodes while the gate voltage transitions from V_g to ground. Given our gate electrode separation (7.4 mm between the extreme grounded screens), a non-negligible volume of particles is located in this region as the voltage is suddenly switched. The pre-gate energy and velocity of these particles may accordingly be smaller than in the original beam, resulting in anomalous energies and flight times, whose effect we have modelled using the measured mass/charge distribution as a model input (section B in the supplementary material). The results of this model are included as dashed lines in figure 11, confirming that the finite gate gap yields a signal with decreasing regions similar to those observed.

Although this model does a fair job at rationalizing the observed decreasing signals, it is not good enough to provide an artefact-free correction. In particular, it fails to follow the slower decay at $\sim 300 \mu\text{s}$. This artefact will accordingly introduce a modest ambiguity in our characterization of the drops.

4.4. Ions

The analysis of the fastest particles ($\tau < 40 \mu\text{s}$) must be carried out without a moving average in time. The process of fitting the data to a set of error functions is nonetheless

Probing electrically driven nanojets

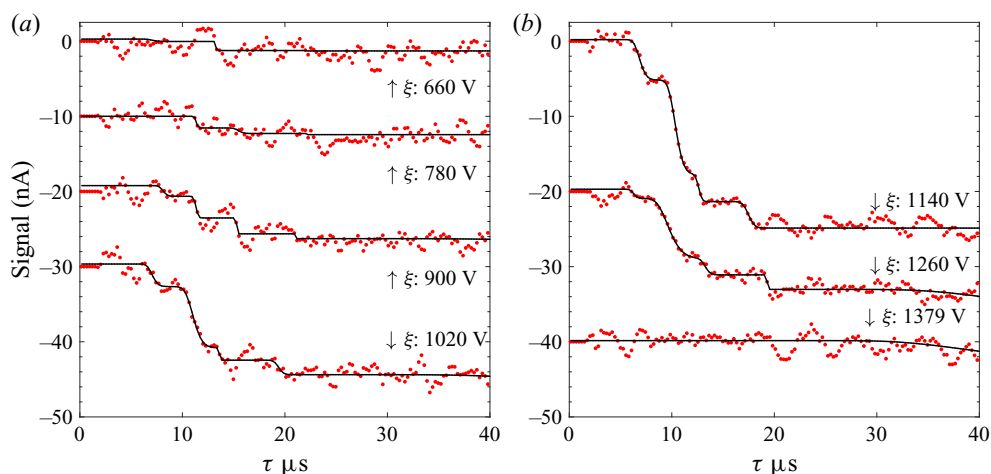


Figure 12. Data (dots) and fit (solid lines) for the TOF measurements from ions at seven selected energies with the presence of ionic species. Note that each consecutive energy (top to bottom) is shifted vertically by -10 nA in (a) and -20 nA in (b).

B_1	m_1^-	B_2	m_2^-	B_3	m_3^-	B_4	m_4	m_5	m_6	m_7	m_8	B_5
250	445	660	1001	1100	1557	1820	2113	2669	3225	3781	4337	4380

Table 4. The m/q boundaries B_j (atomic units) used for locating the various ionic steps, and cluster ion masses m_i for singly charged negative ions from the monomer to the octamer. Masses m_4 – m_8 are combined in a single broad step.

facilitated by the fast rise of the current in this region. As shown in figure 12 the dimer peak is clearly resolved at energies in the vicinity of those at which its height in the TOF curves is maximal. The signals for the monomer and trimer ions are weaker and involve greater ambiguity. The TOF curves continue rising at m/q larger than corresponding to the trimer, although without recognizable steps associated with specific clusters. To account for five of these larger clusters (tetramers to octamers), an additional broad step has been introduced spanning the range $1820 < m/q < 4380$ (atomic units). The process of determining optimal fitting parameters b_i for the ions is facilitated by the fact that their mass/charge ratio is known exactly, whence the centre of the step must lie on a line in the plane $(1/\xi, 1/u^2)$ given by (4.2a) as $1/\xi = (1/u^2)(2q/m)$, with fixed slope $2q/m$. Accordingly, we divide that plane into regions separated by lines going through the origin, with slopes intermediate between those for the monomer, dimer, etc. The boundary slopes used to separate the allowed search regions for the various steps of clusters or cluster groups are shown in figure 13(a). Their m/q are also collected in table 4 as the quantities B_i , together with the theoretical masses for the first eight singly charged negative cluster ions. Figure 12 also shows the locations of the steps identified in the given TOF curve at energy ξ .

Fitting the experimental data via (4.7) with the constraint that the c_i be within the permissible domains (table 4) we obtain values for coefficients b_i , c_i and d_i for each of the experimental energies (table 5). The resulting mean ion velocity u is represented versus ξ in the $(1/u^2, 1/\xi)$ plane of figure 13(a), where the size of the symbols is proportional to the step height b_i .

ξ (V)	Monomer			Dimer			Trimer			Ion rest		
	b_1 (nA)	c_1 (m s ⁻¹)	d_1 (m s ⁻¹)	b_2 (nA)	c_2 (m s ⁻¹)	d_2 (m s ⁻¹)	b_3 (nA)	c_3 (m s ⁻¹)	d_3 (m s ⁻¹)	b_4 (nA)	c_4 (m s ⁻¹)	d_4 (m s ⁻¹)
540	0.00	12537	20.3	0.00	9681	1114.5	-0.30	8110	12.9	0.00	7095	12.9
660	-0.22	18951	54.5	-1.24	12069	31.5	0.00	8507	12.9	-0.06	7265	9.6
780	0.00	17559	94.4	-1.78	14183	181.4	-0.70	10144	38.3	-0.22	7089	12.6
900	-1.33	19699	789.3	-2.88	14186	226.0	-2.11	10525	28.1	-0.63	7631	5.3
1020	-3.05	22767	1412.0	-8.15	14514	868.0	-1.64	11797	46.2	-1.95	8281	167.3
1140	-5.38	23343	1632.6	-12.57	15479	874.2	-3.60	12726	245.8	-3.60	9181	258.4
1260	-1.26	25586	1149.1	-8.03	16502	1651.1	-2.13	12114	353.4	-1.92	8328	16.3

Table 5. Data obtained from the fits for the ions (figure 12).

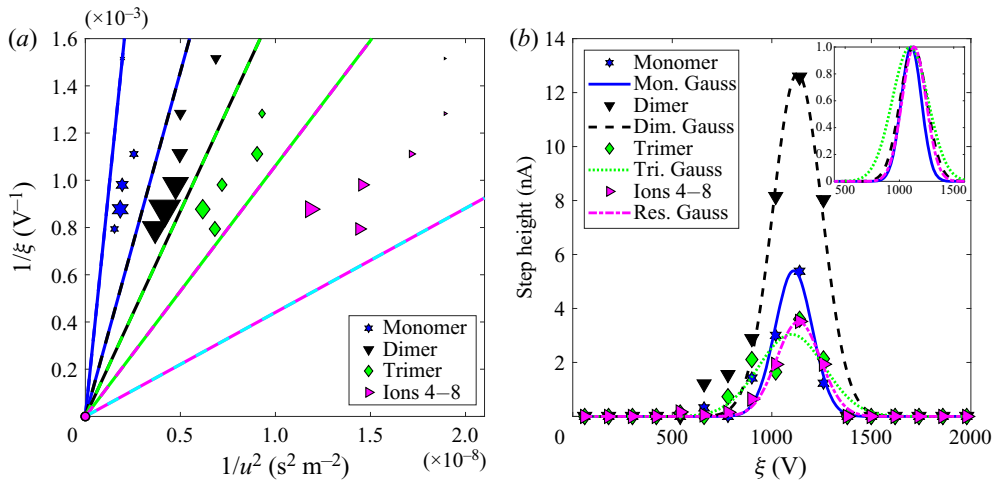


Figure 13. (a) Relation between mean velocity and energy for four ion classes studied. The straight lines shown mark the permissible boundaries within which the centres of the steps fitting the data are allowed (table 4). The area of the symbols is proportional to step height. (b) Step height vs energy for the species identified in (a), with a Gaussian fit added. The inset compares the height-normalized fits. The centres of the Gaussians are at 1116, 1129, 1099, 1135 V for the monomer, dimer, trimer and the heavy ion step, respectively.

Figure 13(b) represents the step height versus the mean energy $b_i(\xi)$ for the four ion classes analysed. The energy distribution for the dimer ion has a full width at half maximum (FWHM) of approximately 300 V. These widths diminish when analysed separately for the various collector angles (section C in supplementary material), but are nevertheless larger than what could be due to experimental limitations or data processing effects. Most of this spread is accordingly genuine, as confirmed by the fact that the data in figure 13(a) fall along a line with the expected $2q/m$ slope.

Of considerable interest is the fact that the mean ion energy measured here agrees closely with the jet breakup potential, to be later determined by analysis of the drops. This shows that the ions must originate either directly from the jet breakup region, or shortly downstream from it, released by the drops. This behaviour has been previously reported by Gamero-Castaño (2008) for a different IL (1-ethyl-3-methylimidazolium bis(trifluoromethylsulfonyl)imide; EMI-Im) having lighter anions, higher electrical conductivity and a smaller viscosity than EMI-FAP. Less viscous and more conducting electrolytes often eject ions from the base of the jet, which are readily recognized because their energies are close to the emitter potential.

4.5. Drops

We now analyse the TOF data in the droplet region ($\tau > 40 \mu\text{s}$; figure 14) by fitting them to a combination of one two or three error functions using $n = 2$ in (4.7).

4.6. Main drops

The most substantial feature seen in figure 14 is a step that first arises at 1260 V and at approximately 100 μs , evolves to larger flight times at increasing energies, peaks at 1500 V and decays at 2099 V to a small height centred at 250 μs . This dominant structure evidently corresponds to the main drops produced by the jet breakup. The characteristic

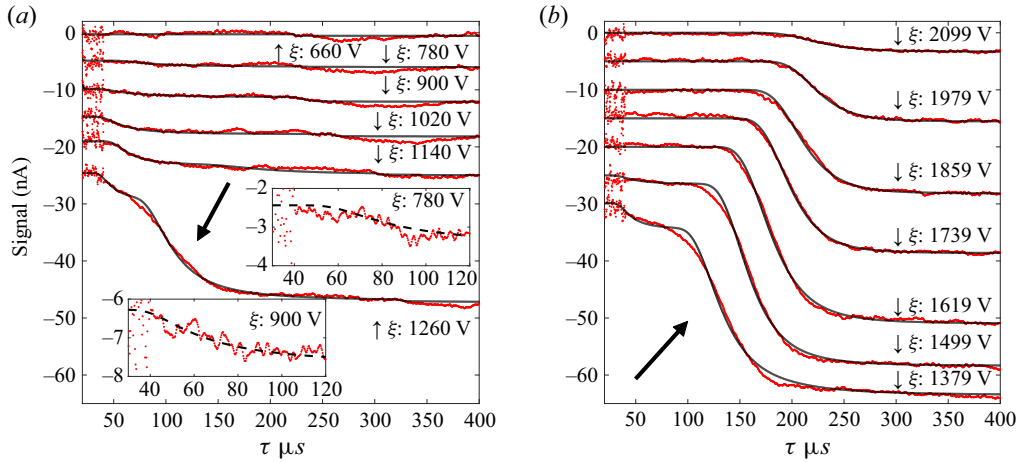


Figure 14. Fitting (black line) of the data (colored dots) to (4.7) at energies including droplet signal. The fitting uses a single error function at energies above 1500 V, where the secondary retrograde step at the highest time visually extinguishes. All data include a 10 μs moving average. The signal from the fast droplets is dominant from 780 to 1140 V, is comparable to that from the other drops at 1260 V and becomes imperceptible above 1260 V. Details at $\xi = 780$ V and 900 V show clearly the onset of the appearance of fast drops.

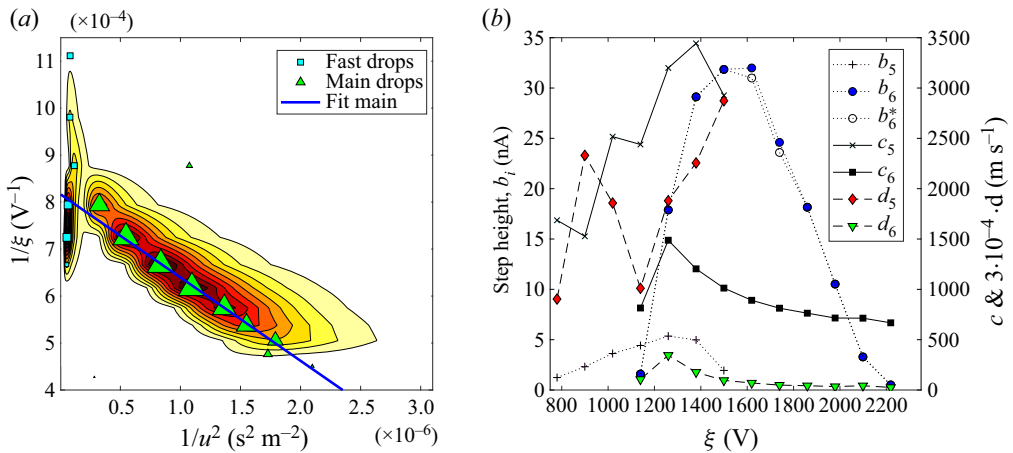


Figure 15. (a) Differential representation of the fits to the data from figure 14 for main and fast droplets. The symbols indicate the positions of the local maxima in the horizontal variable and their area is proportional to step height. The solid line is a linear fit through the high-abundance region for the main drops. (b) Energy dependence of the parameters b , c , d defining the error function fits. Open circles are corrected, filled circles uncorrected. The b_6^* coefficient represents the actual value used for the error function fit including the retrograde effects. The b_6 coefficient presented has been slightly increased to include the signal lost due to the retrograde step.

step parameters b , c , d for these main drops are shown in figure 15(b). The two lines shown (b_6 and b_6^*) account for the ambiguity associated with the uncorrected retrograde signals, involving some ~ 2.5 nA. In the corrected data the step height at certain energies is increased by a value similar to the overall retrograde region loss, in a way that the curves at the highest energies (least likely to suffer from retrograde effects) closely match the experimental data. Subsequent data analysis for the main drops will use the corrected data, with correction shifts given in table 6.

Probing electrically driven nanojets

ξ (V)	Fast droplets			Droplets		Retrograde		Corrector (nA)		
	b_5 (nA)	c_5 (m s ⁻¹)	d_5 (m ² s ⁻²)	b_6 (nA)	c_6 (m s ⁻¹)	d_6 (m ² s ⁻²)	b_7 (nA)		c_7 (m s ⁻¹)	d_7 (m ² s ⁻²)
60–420	—	—	—	—	—	—	—	—	—	—
540	—	—	—	—	—	—	-0.37	765.67	1.34E+04	0.00
660	—	—	—	—	—	—	-0.21	719.86	7.60E+03	0.00
780	-1.21	1781.6	4.47E+06	—	—	—	-0.19	704.17	6.06E+03	0.00
900	-2.33	1527.2	7.86E+06	—	—	—	-0.69	699.32	3.22E+04	0.00
1020	-3.61	2504.2	5.94E+06	—	—	—	-0.39	612.44	8.26E+03	0.00
1140	-4.39	2406.9	3.36E+06	-1.55	814.7	3.47E+05	-0.21	528.89	2.31E+03	0.00
1260	-5.36	3221.2	6.48E+06	-17.91	1487.3	1.15E+06	-0.33	495.72	4.54E+03	0.00
1379	-4.95	3460.2	7.68E+06	-29.15	1203.4	5.94E+05	-0.16	705.23	1.29E+05	0.00
1499	-1.70	2380.6	6.74E+06	-31.74	1011.9	3.18E+05	—	—	—	0.00
1619	—	—	—	-30.94	890.2	2.31E+05	—	—	—	-1.00
1739	—	—	—	-24.36	818.4	1.70E+05	—	—	—	-1.00
1859	—	—	—	-17.86	759.6	1.39E+05	—	—	—	0.00
1979	—	—	—	-10.51	714.8	1.15E+05	—	—	—	0.00
2099	—	—	—	-3.28	714.5	1.44E+05	—	—	—	0.00
2219	—	—	—	-0.50	666.7	8.24E+04	—	—	—	0.00
2339	—	—	—	-0.06	725.5	2.30E+05	—	—	—	0.00

Table 6. Data obtained from the fits for the droplets, including the retrograde region (figure 14). The ‘Corrector’ column is a proposed addition to the b_6 value to account for the overall signal loss on the retrograde region.

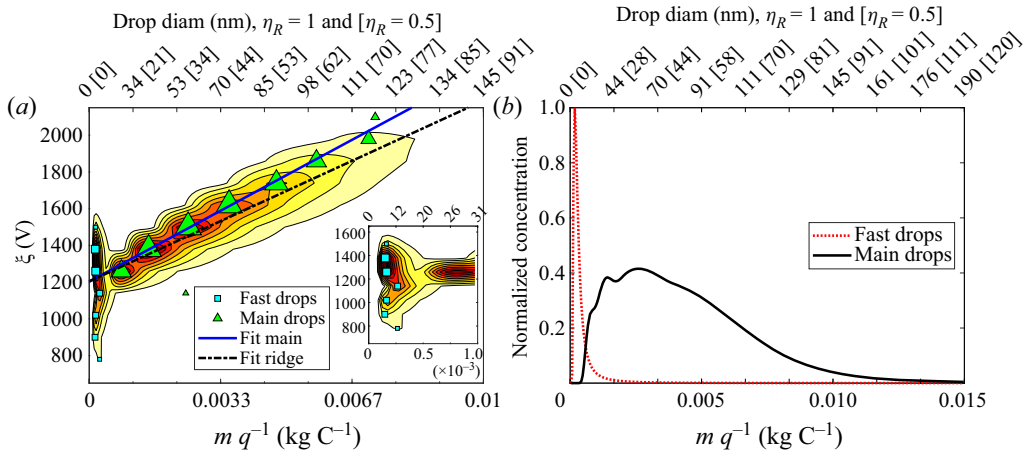


Figure 16. (a) Differential current distribution of all droplets (main and fast) versus mass/charge ($m/q = 2\xi u^{-2}$) and energy. The symbols mark the points of maximal probability at fixed ξ for main and fast droplets. The lines correspond with linear fits to the main drop symbols (solid line) and to the path of minimum slope to the peak (ridge, dash dot). The inset magnifies the fast drop region. (b) Separate m/q distributions for the main and fast drops.

4.7. Fast drops

In addition to the main drops, there is a small but clear step of much faster (smaller) drops appearing at flight times between 60 and 80 μs . This step is anomalous, as it arises at energies below or close to that of the ions, while all other drops have energies clearly larger than those of ions. For instance, the two insets to figure 14 show undoubtedly the presence of small fast drop steps at $\xi = 780$ and 900 V. This step becomes more evident at 1020 and 1140 V, right before the main drop step emerges. The determination of the parameters b , c , d in (4.7) for the fast drops becomes more problematic at $\xi = 1260$ V, when main and fast drops coexist. However, a fast drop step is unambiguously present at 1260 V: even though the quality of the fit is inferior at this than at any other energy, the fit would be much worse if only one error functions was used. This datum gives the highest fast drop current, although with highest uncertainty. The fast drops remain present at 1379 V, when the two distributions are well resolved because the respective step centres are farther apart from each other. At higher energies the main drop step moves further to the right, making the two steps even better resolved. Therefore, the absence of the high velocity step at 1499 V and beyond assures us that the energy distribution of these fast drops has decayed essentially to zero. In other words, in spite of the overlap of both distributions at 1260 V, they are well resolved at all other energies and a complete description of the high energy decay of the fast drop distributions is possible (+symbols in figure 15b). The low energy tail of the distribution of the main drops can similarly be seen in figure 14 to have decayed to a negligible value at $\xi = 1140$ V. This decay is hence also well described by our data, as indicated in figure 15(b) by the filled circle at 1260 V. This makes sense since there is no mechanism for the main drops to be produced at energies smaller than those of ions. In summary, we can determine separately the complete energy and mass/charge distributions of main and fast drops, as shown in figure 16. The peak m/q for the fast drops is ~ 0.0002 kg C^{-1} . Fast drops have been similarly reported by Gamero-Castaño & Cisquella-Serra (2021) for EMI-Im sprays, with the notable difference that their energy distribution reached values up to the those observed for the most energetic drops.

The combination of the high velocity and the low energy of the fast drops yields a rather small m/q , which we shall see is associated with drop sizes considerably below the jet diameter. These fast drops must accordingly be either the product of Coulomb fissions of larger drops, or satellite drops produced during the jet breakup process. It is possible to reject the second of these two alternatives, as satellites form typically in numbers comparable to the main drops (i.e. figure 5 of Tang & Gomez 1994), and carry much less overall charge. In contrast, the daughters from one Coulombic explosion of a conducting drop are numerous, and collectively may carry as much as half the original parent drop charge (Richardson, Pigg & Hightower 1989). The Coulombic fission of all primary (much larger) electrosprayed drops can be visualized in some splendid images reported by Yang *et al.* (2014, figure 4d), where a periodic jet breakup was electrically forced with an external harmonic perturbation.

There is finally a spurious step associated with the retrograde signal previously discussed which we include in the analysis of the data but whose characteristics are irrelevant. The parameters for the three step functions are collected in table 6.

4.8. Determination of jet characteristics

Figure 15(a) represents the differential drop current distribution constructed based on the fits inferred at all available energies for the main and fast droplets. At each energy we have an error function (4.7), whose derivative with respect to the horizontal variable u^{-2} is

$$dI(\xi, u) = \frac{b(\xi)}{\sqrt{2\pi} d(\xi)} \exp\left[-\frac{(u^2 - c(\xi)^2)^2}{2d(\xi)^2}\right] u^4 \xi^2 d \frac{1}{\xi} d \frac{1}{u^2}. \quad (4.8)$$

The maximum of this distribution for given ξ provides an approximately linear relation $\xi^{-1}(u^{-2})$ (triangles in figure 15a), whose slope and y intercept yield the jet breakup velocity and potential according to (4.2c).

An alternative representation of this current distribution in terms of the variables ξ and $m/q = 2\xi/u^2$ is also of interest (4.9), and is depicted in figure 16

$$dI(\xi, m/q) = \frac{\sqrt{\frac{2}{\pi}} b(\xi)}{d(\xi) \left(\frac{m}{q}\right)^2} \exp\left[-\frac{\left(2\xi \left(\frac{m}{q}\right)^{-1} - c(\xi)^2\right)^2}{2d(\xi)^2}\right] \xi d\xi d \frac{m}{q}. \quad (4.9)$$

The position of the ridge in this figure falls on an approximately straight line, as expected from (4.6). Its y intercept gives $V_j = 1205$ V, while its slope $m = U_j^2/2$ yields $U_j = 444$ m s⁻¹ (b line in table 7). To illuminate the level of ambiguity of this determination two alternative calculations of U_j , V_j and ΔV are included in lines c and d of table 7, based on the two additional regression lines included in figures 15(a) and 16(a).

The fraction of mass flow rate and thrust at each energy can be calculated by numerical integration of (4.9) as described in (4.10) and (4.11). The overall drop flow rate and thrust are obtained by adding the partial values across all energies. This method can yield the

	U_j (m s ⁻¹)	V_j (kV)	d_j (nm)	ΔV (V)	ΔT (°C)	\dot{m}_{TOF}^a (μg s ⁻¹)	I_{sp} (s)	T^u (μN)	η_{poly} (%)	I_{TOF} (nA)
<i>b</i>	444	-1.20	48.13	-5.7	-1.06	0.8817	88.04	0.76	65.3	-253
<i>c</i>	480	-1.20		-80						
<i>d</i>	465	-1.22		-70						

Table 7. Jet breakup parameters (velocity, potential, diameter, irreversible voltage drop (4.1) and associated temperature rise) inferred from the distribution of drop velocity and energy, and propulsive parameters for the spray calculated using (4.10) to (4.13). The jet potential and velocity have been extracted from the ridge on figure 16(a).

^aMass flow rate and thrust have been scaled by 1.21 to compensate for the disparity between I_{TOF} (max corrected nA) and emitted current. This correction assumes that all of the missing signal is species independent.

^bRidge of figure 16(a).

^cContinuous line in figure 16(a).

^dRegression line in figure 15(a).

mass fractions for each species

$$\dot{m} = \sum_i \int \frac{m}{q} dI(\xi_i, m/q), \tag{4.10}$$

$$T = \sum_i \int u \frac{m}{q} dI(\xi_i, m/q) = \sum_i \int \left(2\xi_i \frac{m}{q}\right)^{1/2} dI(\xi_i, m/q). \tag{4.11}$$

Ion properties are calculated using their nominal m/q , with b_i and c_i instead of dI and u , respectively. Therefore $\dot{m} = \sum_i (m/q)b_i$; $T = \sum_i c_i(m/q)b_i$. In any case, all contributions other than those from the main drops are negligible in mass flow and fairly small in thrust. The overall flow rate and thrust are obtained by adding the contribution from each species.

Specific impulse and polydispersity efficiency are defined as

$$I_{sp} = \frac{T}{\dot{m}g}, \tag{4.12}$$

$$\eta_{poly} = \frac{\frac{1}{2}\dot{m}(I_{sp}g)^2}{V_o I_e}. \tag{4.13}$$

If one were to replace V_o by V_e in (4.13) one would obtain the thruster efficiency. In our case, where the difference between V_e and V_o is not measurable, $\eta_{poly} = \eta_{thruster}$. More fundamentally, η_{poly} is defined as the ratio between the power actually consumed to achieve a given mass flow rate \dot{m} and thrust T to the minimal power required to obtain them. This minimal power is attained for a monodisperse plume containing a unique q/m , when one readily sees that $P_{min} = T^2/(2\dot{m})$. It is clear that the presence of ions and fast drops decreases this efficiency because they consume a power proportional to their current yet achieve almost no thrust.

4.9. On the distribution of drop velocities

We believe the measured distributions of velocities and energies for particles of given m/q are real rather than a by-product of our finite energy resolution. The question is, what causes these widths? The observed distribution of ξ measured for dimer ions $b_2(\xi)$ could be due either to (a) the distribution of V_j resulting from temporal variability of the position

of the breakup point, or rather (b) to other sources of randomness, especially the fact that the breakup process is not periodic, so energy conservation is not strictly applicable. We shall here assume hypothetically scenario (a) to show that it is incompatible with our data. In that hypothesis, the measured ion energy distribution would coincide with the distribution of jet breakup potentials

$$P(V_j) = b_2(V_j). \quad (4.14)$$

From this distribution one may now infer the distribution of drop energies and velocities, since the jet velocity U_j and electrical potential V_j are linked by the equation of energy conservation (4.1), which applies down to the jet breakup point. Therefore, unless there is an additional source of particle velocity fluctuation, the probability distributions of U_j and V_j should be simply related. Accordingly, we write the particle velocity from (4.6) as

$$u^2 = [V_o + V_j(1/\alpha - 1)]2q_j/m_j. \quad (4.15)$$

This equation predicts indeed a variation in u^2 as a result of variations in V_j . However, the sensitivity of u^2 to changes in V_j is proportional to $(\alpha^{-1} - 1)$ and vanishes when $\alpha = 1$. According to (4.6), this condition corresponds also to a unique particle energy, $\xi = V_o$. Therefore, if the main source of particle velocity dispersion at fixed energy were the dispersion in jet breakup potential, there would be no velocity dispersion at the mean energy. In our measurements (see section C of supplementary material for higher energy resolution), however, drops with this special energy exhibit a velocity spread comparable to that of drops with other energies. From this we cannot but conclude that the mechanism responsible for the observed spread in velocity in approximately monoenergetic drops is not just due to the variation in U_j and V_j associated with the randomness in the position of the jet breakup point. A more probable explanation for the observed spread in velocities is that it is substantially due to unsteadiness in the process of drop production. It would therefore persist even if the breakup point were exactly fixed. If the jet was periodically excited close to the most unstable frequency for drop production, such that drops of a fixed volume would be delivered in each period, all drops would also acquire the same energy. However, since drops of widely different sizes are produced in each pinching of the jet, with different intervals between successive pinchings, the breakup process is capable of injecting different energies and velocities even into identical drops, depending on the sizes of the neighbouring drops produced either before or after. In other words, energy is conserved in our unsteady processes only on the average, but not for each individual drop. Therefore, understanding the observed velocity, size or charge distributions of the drops will require modelling the unsteady breakup process.

The special situation encountered at $\xi = V_o$ of a velocity insensitive to fluctuations in V_j makes intuitive sense, as V_o may be viewed as the total energy available to accelerate first the jet from zero initial kinetic energy, and then to further accelerate the drops to their final energy. Drops having an energy equal to V_o also have the same charge/mass as the jet: $q/m = Il/(\rho Q)$, and are accelerated to exactly the same final velocity whether they are in jet form or drop form. Therefore, their final velocity cannot be affected by changes in the position of the breakup point

4.10. Comparison of observed and expected jet parameters

4.10.1. Jet breakup characteristics

Comparisons are made in table 8 between our results for EMI-FAP and those of Gamero-Castaño (2008) for the different IL EMI-Im and for numerous electrolytes of

	Liquid	D_j/r_G^d	D_j/L^e	$\rho KQ/(\gamma \epsilon_0)$	$I/(\gamma KQ)^{1/2}$	$1/Re^f$	$\Delta V(kV)^g$
EMI-FAP ^a	highrescal5 (19.6 °C)	0.530	0.348	2010	2.72	215	1.190
	tempstudy2 (35 °C)	0.550	0.362	1820	2.21	142	0.639
	tempstudy3 (45 °C)	0.557	0.376	1168	3.79	109	0.458
EMI-Im ^b		0.459–0.569	0.326–0.344	390–11290	3–4.09	128	0.575
TBP ^c		0.426–0.506	0.366–0.444	42–171			

Table 8. Characteristics of our jets compared with prior work.

^aPresent study. ^bGamero-Castaño (2008). ^cGamero-Castaño and Hruby (2002). ^dEquation (4.16a). ^eEquation (4.16b). ^fEquation (4.17d). ^gEquation (4.17a–c) with $\epsilon = 8.9$, $\alpha(8.9) = 5.33$, $\beta(8.9) = 1.92$.

tributyl phosphate (TBP). The table relies on the following definitions:

$$r_G^6 = \rho \epsilon_0 Q^3 / (\gamma K); \quad L^9 = \rho^2 Q^5 \epsilon_0 / (K \gamma^2); \quad L/r_G = [\rho K Q / (\gamma \epsilon_0)]^{1/18}, \quad (4.16a-c)$$

and shows that the two ILs operate in comparable regimes. The characteristic length r_G originally used by Gañán-Calvo (1997) has been shown by Gamero-Castaño & Hruby (2002) to provide a suitable scale for the jet breakup diameter in their measurements with electrolytes of tributylphosphate. The value of r_G also provides a length scale that collapses into very similar shapes a number of numerical calculations of cone jets (Gamero-Castaño 2010; Gamero-Castaño & Magnani 2018). The alternative scale L in (4.16b) is suggested by the asymptotic form proposed by Gañán-Calvo for the jet diameter d_j as a function of the axial distance z to the apex of the cone: $D^4 z^{1/2} = C$ (i.e. (19) of Gañán-Calvo *et al.* 2018), where the constant C naturally defines the new length scale as $L^{9/2} = C$. Note from (4.16c) that the lengths r_G and L have comparable numerical values because they are related through a very small (1/18) power of the dimensionless parameter $\rho K Q / (\gamma \epsilon_0)$, which is never particularly large or small.

4.10.2. Irreversible voltage drop

Given the potential of the jet at the meniscus base and its mean value at the breakup point, the irreversible potential drop may be determined from (4.1) using the mean jet velocity. This quantity is presented in table 7 and turns out to have an unphysical negative value. The corresponding jet temperature change, if substantial, would have drastic effects on fluid properties. For instance, while glycerol electrolytes have insufficient conductivity to evaporate ions, they do nevertheless produce ions when run at sufficiently high voltage (Cook 1986). More remarkably, Fedkiw & Lozano (2009) have shown that the singularly viscous and poorly conducting IL 1-butyl-3-methylimidazolium iodide is able to operate in the purely ionic regime of emission. A simple explanation for these anomalies is that dissipation increases the tip temperature sufficiently to produce local electrical conductivities adequate for ion evaporation. The temperature change due to dissipative losses may be obtained from the emission current, the mass flow rate and the assumption that the unknown heat capacity of EMI-FAP is similar to that of the related ionic liquid 1-butyl-3-methylimidazolium tris(pentafluoroethyl) trifluorophosphate (BMI-FAP) ($c_p = 1193 \text{ J kg}^{-1} \text{ K}^{-1}$ (Safarov *et al.* 2017)) as $\Delta T = (\Delta VI / c_p \dot{m}) = -1.06 \text{ C}$, by assuming that all of the electrical energy dissipated is transformed into heat, and that there are no losses to the environment. These unphysical negative losses are nevertheless small compared with the uncertainties in our experiment, including a 120 V discretization of the energy, and typical drop energy distributions widths of several 100 V. Furthermore, as

seen in [table 7](#), our determination of the jet breakup potential involves errors of tens of Volts. This limited precision precludes determining reliably the temperature rise in our relatively thick jets, but should be adequate for more dissipative jets.

Gamero-Castaño (2008) reports jet breakup velocities U_j and voltages V_j , for the IL EMI-Im. The irreversible voltage drop calculated from his [table 1](#) as $V_e - V_j - \frac{1}{2}\rho QU_j^2/I$ gives values very close to zero, evidently because V_j was obtained directly from the measured ion energy, but U_j was inferred indirectly by assuming a reversible acceleration. Gamero Castaño (2010) has investigated numerous electrolytes of three organic solvents of relatively low viscosity, under a variety of electrical conductivities and flow rates. He concluded that

$$\Delta V = V^*F(\varepsilon); \quad V^* = \gamma^{2/3}/(K^{1/3}\varepsilon_0^{1/6}\rho^{1/6}); \quad F(\varepsilon) = [\alpha(\varepsilon) + \beta(\varepsilon)/Re]; \quad Re = (\rho\varepsilon_0\gamma^2/K)^{1/3}/\mu, \quad (4.17a-d)$$

where ε_0 is the dielectric constant of the liquid, and the range of Re^{-1} covered varied from approximately 0.15 to 5. The quantities α and β in (4.17c) take values of order unity for the range of dielectric constants investigated, which varied from approximately 8.9 to 111. The values of $1/Re$ and V^* for EMI-Im and EMI-FAP at room temperature are collected in [table 8](#). The dielectric constants for these two ILs are unknown, but should be comparable to that of tributyl phosphate, for which Gamero-Castaño reports $\alpha(8.9) = 5.33$, $\beta(8.9) = 1.92$. Equation (4.17) applied to the ILs would predict $\Delta V = 997$ V and 575 V for EMI-FAP and EMI-Im, respectively. These values are vastly larger than what we have measured here, suggesting that (4.17) does not apply to EMI-FAP. A possible reason for this discrepancy is that our Re is well below the range studied by Gamero-Castaño (2010). An investigation with electrolytes of more viscous fluids would help clarify the matter. Another possibility is that perhaps neat ILs behave differently from electrolytes containing modest salt concentrations.

Our conclusion on the inapplicability of (4.17) to ILs is confirmed by a recent study on EMI-Im (Gamero-Castaño & Cisqueña-Serra 2021) reporting independently measured jet breakup velocities and potentials at the centre of the beam. From their tables we infer ΔV values from 40 to 180 V, one order of magnitude below the extrapolation from (4.17). In spite of a considerable scatter in these data, ΔV increases markedly with Q , in sharp contrast with the prior striking observation on the independence of ΔV on Q for electrolytes of organic solvents. In summary, both ILs exhibit a much smaller level of energy dissipation than suggested by prior work on electrolytes of low viscosity solvents.

4.10.3. Emission potentials

Using the jet velocity from [table 7](#) and assuming it to be constant, the emission potential of the various drops can be calculated. This is done by subtracting the energy gained in the jet from the final energy of the particle. [Figure 17\(a\)](#) reproduces the data of [figure 16\(a\)](#) in terms of the new variables. It is visually clear on [figure 17\(a\)](#) that for the main drops ($m/q \sim > 0.0004$ kg C⁻¹) at higher mass over charge ratios the emission potential has a higher spread. One also sees that the fast drops ($m/q \sim < 0.0004$ kg C⁻¹) display a wider range of emission potentials than the main drops. The source of this effect is discussed below.

4.10.4. Diameter of the drops

While we can infer the breakup radius of the jet $R_j = \{Q/(\pi U_j)\}^{1/2}$, we lack direct information on the radii of the drops. Approximate drop size information may nevertheless be obtained from the fact that a drop of radius R may at most carry Rayleigh's limiting

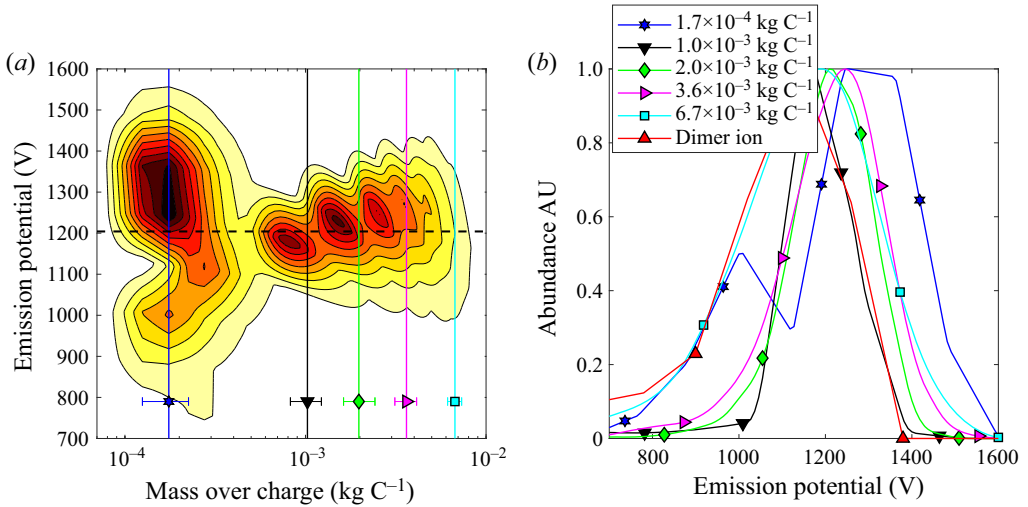


Figure 17. (a) Data of figure 16 with the y axis changed from ξ into $V_E = \xi - \frac{1}{2}(m/q)U_J^2$. (b) Distribution of emission potential V_E at five intervals of mass over charge whose centre and width are marked by the vertical lines and error bars in (a). The emission energy of the dimer ion is also displayed. The FWHM are approximately 440, 180, 220, 260, 370, 300 V following the order of the legend.

charge $q_R = 8\pi(\epsilon_0\gamma R^3)^{1/2}$, where γ is the surface tension of the liquid forming the drop (35.3 dyn cm⁻¹ at room temperature for EMI-FAP, table 1) and ϵ_0 is the electrical permittivity of vacuum. Therefore, Rayleigh’s charge ratio η_R is always less than unity

$$\eta_R = \frac{q}{8\pi\sqrt{\epsilon_0\gamma R^3}} \leq 1. \tag{4.18}$$

We may accordingly write m/q in terms of R and η_R only, or alternatively express the drop radius in terms of the experimental quantity m/q as

$$R = (m/q)^{2/3}(36\eta_R^2\epsilon_0\gamma/\rho^2)^{1/3}. \tag{4.19}$$

Therefore, except for an ambiguity in the factor of order unity $\eta_R^{2/3}$, the m/q information included in figure 16 can be converted into drop radius information. This is done for the drop diameter in the upper horizontal scales of figure 16 for the representative cases where the Rayleigh ratio is either 1 or 1/2.

When $\eta_R = 1$ the fast drops have a mean diameter of 10.7 nm. The associated surface electric field is 1.7 V nm⁻¹, sufficient to evaporate ions. However, fast drops cannot be the source of most of the ions observed because the total ion current exceeds threefold that of fast drops. Nevertheless, the Coulomb explosions yielding these fast drops involve the formation of transient jets on the main drops having diameters about half the diameter of the fast drops (5 nm). These jets would naturally also support electric fields adequate for ions to evaporate, not only from their tip, but predominantly from their neck region, with associated currents that could be up to half the current originally carried by main drops. Furthermore, because the main drops would originally carry most of the jet current, while ions represent approximately 1/4 of the total, it is certainly possible that most ions would be released from exploding main drops. This scenario would demand the fission of a substantial percentage of the main drops, a situation that has been previously demonstrated by Yang *et al.* (2014), even for 100 % of the main drops. Their outstanding images confirm

also that the jet produced during the transient fission of the main drops is approximately half the diameter of the daughter drops, and much smaller than the main jet diameter. The notion that ions are evaporated from fissioning main drops slightly downstream from the breakup point is also compatible with the observation that ion energies (~ 1130 V) are modestly but clearly below the jet breakup potential (~ 1205 V). [Figure 17\(b\)](#) provides further evidence for this fissioning. The FWHM of the emission potential for relatively large drops having mass/charge = 0.0067 kg C^{-1} is more than twice that at 0.001 kg C^{-1} . This wider distribution is expected if most or all of these large drops had undergone a Coulombic explosion within a range of positions, ultimately causing a higher spread of emission potentials. An additional indication of the high probability that the large drops would explode is given by the ratio of electrostatic to capillary stresses on the jet, $\Psi_j = I_j^2 d_j^3 / (64Q^2 \gamma \epsilon_0)$, which for our jet takes a value 0.806, relatively close to unity. Let us now assume that the average drop radius R_D is a factor η_D larger than the jet radius, and that the charge over mass of the average drop is the same as that of the jet. Then, the ratio of electrostatic stresses to capillary stress on the average drop is $\Psi_D = \Psi_j (2\eta_D^3 / 9)$. Taking η_D to be 1.89, as in Lord Rayleigh's inviscid breakup of a neutral jet, results in $\Psi_D = 1.5\Psi_j$, which for our jet gives $\Psi_D = 1.21$. Our drops are therefore estimated to be on the average charged above the Rayleigh limit, so it makes sense that a substantial fraction of them would undergo either Coulomb explosions or ion evaporation.

4.10.5. Broad drop mass/charge range

The following discussion will be based on information obtained from energy and velocity distributions, without corrections for discrepancies with our bulk measurements of current and liquid flow rate. Note that our experimental technique measures energy and velocity (and m/q) for the drops after complete acceleration past the extractor. Accordingly, we do not have direct information on their properties prior to any event of ion evaporation or Coulomb explosion, which take place much before the acceleration is completed. The m/q distribution of [figure 16\(b\)](#) is evidently quite broad. This does not necessarily imply that the mass distribution is also broad, since the dispersion in m/q could conceivably be largely due to dispersion in q . Nevertheless, for present purposes we shall convert m/q into mass or size under the assumption $\eta_R = 1$. Taking as reference the values of m/q at which the height of the m/q distribution is half the maximum ($m/q \sim 6.9 \cdot 10^{-3}$ and $6.2 \cdot 10^{-2} \text{ Kg C}^{-1}$), the corresponding drop sizes range from 24 to 105 nm. Given our jet diameter of 48 nm, and assuming a ratio of mean drop to jet diameter of 1.89 (as in Lord Rayleigh's inviscid breakup of a neutral jet), we would expect a mean drop diameter of 90 nm. This value is coherent with the upper range of our measured distribution. The presence of 24 nm drops with diameters half the jet diameter could conceivably be attributable to the production of satellites at the jet breakup. However, rather than two drop classes, we have a broad continuous distribution covering sizes from 24 to 105 nm. This situation is typical of electrosprays run at relatively high flow rates, as well as of relatively viscous ILs such as EMI-BF₄ (Romero-Sanz *et al.* 2003), EMI-Im (Gamero-Castaño 2008; Gamero-Castaño & Cisuella-Serra 2021) or EMI-FAP.

4.10.6. Note on missing mass and current

This experiment shows a noticeable mismatch between the emitted and received currents, as well as the emitted and calculated mass flow rates. When subtracting the current and uncorrected mass flow rate values from [tables 2](#) and [7](#) (emission and reception respectively), there is a loss of 54 nA and $0.65 \mu\text{g s}^{-1}$ from emitter to collector. The mean

mass over charge for the unaccounted particles is approximately 0.012 kg C^{-1} . Droplets with this mass over charge ratio emitted from a jet under the conditions from [table 7](#) would have energies slightly above the measurement conditions and would not be captured. To cover this gap we have performed another room temperature experiment under conditions fairly close to those of [table 2](#), with retarding voltages extending to 3 kV. The result confirmed that no particles are present at energies from 2 to 3 kV. Another possible cause for the disparity is accumulation of material in the gate meshes during the experiments. Fluid accumulation reduces the mesh transparency and is particularly relevant around the centre which might receive unusually large droplets during the spray startups previous to the experiment.

4.10.7. Polydispersity and thruster efficiency

An important corollary of the wide range of energies found in the spray is that many previous calculations on propulsive characteristics of electrosprays (which, in the absence of energy information, have tended to assume that all particles have the same energy) may involve considerable errors. In fact, since the initial acceleration of the jet is common for all particle sizes, the role of polydispersity in decreasing η_{poly} is restricted to the electrical potential used to accelerate the drops (V_j rather than V_o). Gamero & Hruby (2002) have encountered situations approaching the limit when V_j is small compared with V_e , in which polydispersity would lead to very little reduction in η_{poly} . A possible strategy to improve propulsive characteristics would then be to identify situations where the jet accelerates to velocities of several km s^{-1} before breakup. On the other hand, if our spray was post-accelerated to voltages that are large compared with $V_o - V_j$, η_{poly} would decrease below the 65 % previously reported.

5. Angular distribution of charged particles in the spray

So far, we have analysed primarily the whole spray, including no angular information. This study has shown that the small extra step arising at large τ is an artefact that may be ignored. As already seen in relation to the central collector ([figure 9](#)), there is sufficient signal to analyse separately most of the collectors to extract information comparable to that obtained for the full spray. This information is reported for collectors 1–7 in section C of the supplementary material. From it we conclude that there is little variation in the angular distribution of the various species, as seen in [figure 18](#). Similarly, we find that the mean energy of the various ions and of the fast drops changes little with polar angle. The width of the energy distributions for all ion classes is obtained with substantial scatter. Within this scatter, it is also relatively independent of the polar angle. Finally, even the 2-D distributions of collected current as a function of particle velocity and energy (or m/q and energy) are obtained with sufficient signal/noise to also extract from them values for the breakup jet velocity and potential. These U_j and V_j show also little angular dependence.

In conclusion, whatever the mechanism that leads to the observed angular spread of the various species in the spray, it seems to be essentially independent of m/q . This observation is compatible with the hypothesis that the chief products of the jet breakup are the main drops. These naturally spread radially by two possible mechanisms: either space charge amplification of any small initial departures from the jet axis for an axisymmetric jet breakup, or as a result from a whipping instability of the jet. Some of these drops explode, producing ions and fast drops having substantially smaller m/q . If released near the axis, these lighter species would tend to spread radially much faster than the main drops (since the axial space charge field is the same for all particles). The fact that they do not segregate

Probing electrically driven nanojets

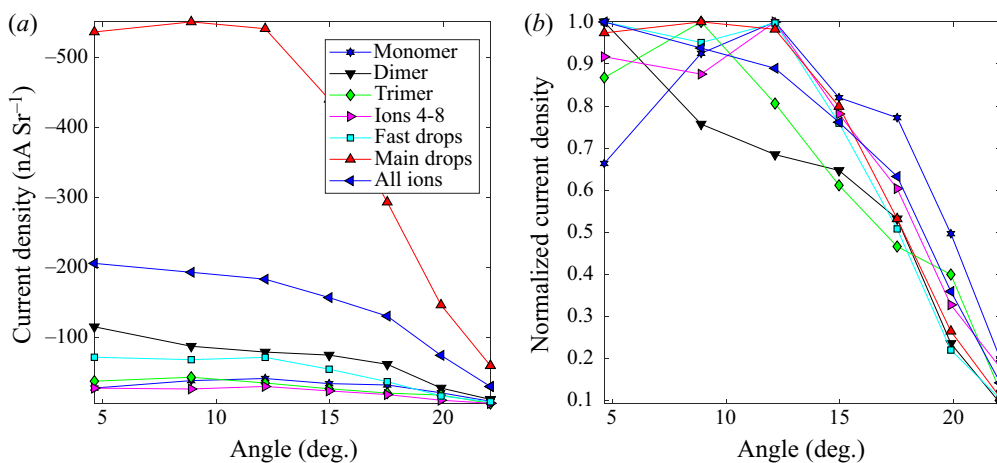


Figure 18. Angular distribution of the current density for the various species (normalized on the right with its maximum value).

radially from the main drops indicates that (i) either the explosions producing them occur when the exploding drops are already far from the axis, where space charge fields have decayed, or (ii) that the dispersion is due to the whipping instability. The first hypothesis is far less likely than the second because a substantial radial dispersion of the main drops by space charge would take time, and the energy of the products would then tend to be less than the breakup potential of the jet. Our jet then appears to be subject to a whipping instability. In future studies we will explore a wider range of liquid flow rates, hopefully including conditions with axisymmetric jet breakup, under which the angular distribution of species may be quite different.

6. Studies at elevated temperatures

Experiments were conducted at several temperatures by locally heating the surfaces surrounding the emission point. This comprises the vacuum flange where the capillary is supported, as well as the extractor plate, whence the emission point is surrounded on all sides by heated elements. The very last 10 mm of the capillary was cantilevered from the support structure and simply surrounded by vacuum. The prior 20 mm were in contact with the support structure, made out of a polyether ether ketone (PEEK) insulator inserted on a large aluminium plate. The aluminium plate supporting the capillary structure and the perforated extractor electrode were both fitted with temperature probes, which revealed that the extractor was approximately 5 °C colder than the plate. The temperature reported for these experiments is the plate temperature. The temperatures remained stable for the duration of the experiments. The upstream portions of the capillary, including its region outside the vacuum chamber and the vial holder, were not heated and therefore remained close to room temperature. At 55 °C the emission became unstable, prior to the end of the experiment (taking ~1 h), precluding its completion. Besides the room temperature measurement previously discussed, two additional experiments were carried out, one at 35 °C and another at 45 °C. The measurement technique and the analysis method were identical in the three cases, with the only difference that the capillary tip for the 35 °C and 45 °C experiments had 40 μm ID and ~15 μm tip diameter, which resulted in lower emission voltages. This new capillary was not calibrated with gas bubbles.

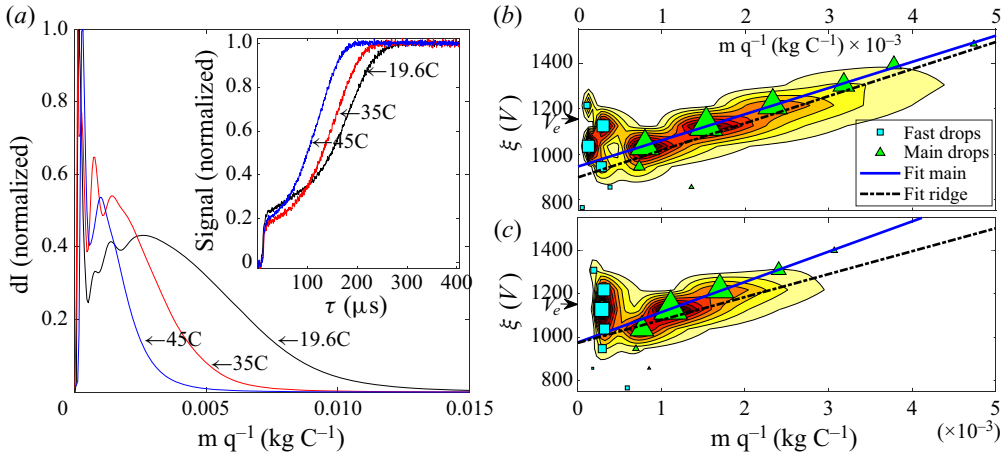


Figure 19. (a) Comparison of the distribution of mass over charge for experiments at three temperatures T . The inset shows, cumulative forms of the TOF curves at the highest measured energy. Panels (b) and (c) are the differential current distributions vs mass/charge at 35 °C and 45 °C.

T (°C)	\dot{m} ($\mu\text{g s}^{-1}$)	ρ^a (kg m^{-3})	K^b (S m^{-1})	μ^b (mPa s)	γ^a (dyn cm^{-1})	V_e (V)	I (nA)	m_j/q_j (kg C^{-1})
19.6	1.38	1716	0.44	75.35	35.32	-1642	-307	0.0045
35	0.76	1698	0.74	40.02	34.51	-1160	-235	0.0032
45	0.37	1685	0.97	28.41	33.98	-1161	-319	0.0011

T (°C)	I_{TOF} (nA)	\dot{m}_{TOF} ($\mu\text{g s}^{-1}$)	Thrust (μN)	I_{sp} (s)	η_p (%)	U_j (m s^{-1})	V_j (V)	D_j (nm)
19.6	-253	0.882	0.76	88.04	65.3	443	-1204	48.13
35	-232	0.403	0.396	100.38	71.85	488.2	-898	33.46
45	-213	0.3481	0.4269	125	64.5	528	-977	22.6

Table 9. Various characteristics of the liquid at the breakup point (density, ρ , electrical conductivity K , viscosity μ , and surface tension γ) for the three sprays studied at three temperatures. The mass flow rate and thrust have been scaled by the ratio of emission current to TOF current.

^aSoučková *et al.* (2012). ^bSeki *et al.* (2012).

Figure 19(a) shows a significant reduction in mass over charge with a relatively modest increase in temperature: the peak of the distribution for the main drops shifts from 0.0025 to 0.001 kg C^{-1} . This is rationalized with the steep variation of the liquid conductivity with temperature, which almost doubles from 23.4 to 45 C. Using the relation $I \propto (\gamma K Q)^{1/2}$ (Fernández de la Mora 2007), doubling the conductivity (K) at fixed spray current halves the flow rate (Q). This in turn, halves the mass over charge ratio on the jet since the liquid density changes little. From table 9, the mean mass over charge for the jet and its diameter decrease with increasing temperature (although not exactly as predicted), therefore producing smaller main drops. The propulsive and material properties of the three experiments are collected in table 9. The specific impulse increases with temperature even with reduced emitter voltages.

7. Conclusions

- We have carried out the first full beam study of an electrospray in a vacuum, where the energy ξ and the velocity u of all charged particles are determined in series. This is also the first study where the intensity of the whole beam is measured as a function of polar angle θ , providing 3-D distributions $I(\xi, u, \theta)$. This angular information enables an accurate determination of the full velocity and energy from a TOF measurement providing only the axial velocity. As a proof of concept of our new experimental technique, only three sprays have been characterized, with each spray studied at a different temperature, all for the IL EMI-FAP in negative polarity. The most detailed study has focused on a spray formed at room temperature with an emitter potential of -1642 V.
- Spreading the limited available signal into the 3-D space (ξ, u, θ) naturally comes at a cost in signal/noise. Accordingly, much of the analysis is carried out by summing up the currents received at all angular locations, as in prior studies. Even so, unlike prior studies, the angular information is now used to achieve much better energy and velocity resolution.
- Particles are found over quite wide ranges of velocities and energies, the latter including values substantially below as well as substantially above the emitter voltage.
- Approximately 20 % of the current is due to ions, mostly the dimer, with separately distinguishable signal for monomers and trimers, and with a globally measurable group of larger clusters from tetramers to octamers. All these ions have energies of approximately 1140 V and must originate from the jet breakup region or shortly downstream.
- A well-defined group of very small drops is identified at anomalously low energies, below that of the jet, and with mass/charge much below that of all other drops. These fast drops are interpreted as products of Coulomb fissions of main drops taking place slightly downstream from the jet breakup region. Their small sizes confirm that the transient jets in the main drops from which they originate are capable of evaporating ions, suggesting that most of the ions referred to in the previous point are also ejected from Coulombically exploding main drops, rather than from the jet upstream the breakup point, or the breakup region itself. Possible alternative scenarios for the production of fast drops have been discussed by Gamero & Cisquella (2021) for sprays of EMI-Im.
- Drops with energies extending broadly from 1200 up to 2000 V constitute the bulk of the spray. The corresponding velocities spread also over a wide range. However, the drop velocities associated with a given energy are narrowly defined.
- The relation observed between the mean drop velocity and energy is well explained in terms of a two-stage acceleration process: first, a voltage drop of about 0.42 kV is used to accelerate the jet as a whole to a final velocity $U_j = 444$ m s⁻¹ and electrical potential V_j of approximately 1.2 kV. Next, by falling from the jet potential V_j down to ground in independent free flight, drops with different mass/charge accelerate to different final velocities and energies. The values reported $U_j = 444$ m s⁻¹, $V_j = -1204$ V are obtained by fitting the experimental relation between drop energy and velocity to the expected relation for this two-step acceleration process.
- Overall, the technique presented here displays some limitations. The electronic noise introduces the need for energy binning and moving averages which reduce the energy resolution. Another critical disruption is the fact that 4.3 % of the particles are within the gating electrodes at the moment of gating. Gating distorts their

energies and velocities, creating an anomalous signal that is difficult to correct and distorts slightly the determined distribution of main drops. Since other methods for stopping the beam do exist this should not be a concerning issue in future studies.

- The angular distribution of the various drop classes and ions found are broadly similar to each other, with no preferred angular positions for any of them.
- Relatively modest changes in temperature ($\sim 20^\circ\text{C}$) result in significant reductions of the jet diameter and the droplet mass/charge distributions under comparable spray currents. This leads to substantial increases in specific impulse, even though the emission voltage has decreased with increasing temperatures. This brief exploration shows the great potential of increasing temperature to improve the propulsive parameters of the jet.

Supplementary material. Supplementary material is available at <https://doi.org/10.1017/jfm.2021.771>. The supplementary material relates to the transmission of the screens (section A), to a model accounting for observed retrograde features (section B) and to the determination of the angular distribution of plume properties by separate analyses of the currents received by individual collectors (section C).

Acknowledgements. We would like to acknowledge C. Mochi and G. Hénaff, for their various contributions to this project. The present text has benefitted from several useful remarks made on an earlier draft by Dr M. Gamero-Castaño.

Funding. This work has been funded primarily through AFOSR grant FA9550-18-1-0165. Early development of the measurement facility was funded by the Air Force Rocket lab (Edwards base) in collaboration with Dr S. Gildea, whose numerous insights are much appreciated.

Declaration of interests. The authors report no conflict of interest

Author ORCIDs.

 Luis Javier Perez-Lorenzo <https://orcid.org/0000-0002-3473-2846>;

 Juan Fernandez de la Mora <https://orcid.org/0000-0002-9077-2877>.

REFERENCES

- BENASSAYAG, G., SUDRAUD, P. & JOUFFREY, B. 1985 In situ high voltage tem observation of an electrohydrodynamic (EHD) ion source. *Ultramicroscopy* **16** (1), 1–8.
- COLLINS, R.T., SAMBATH, K., HARRIS, M.T. & BASARAN, O. 2013 Universal scaling laws for the disintegration of electrified drops. *Proc. Natl Acad. Sci. USA* **110** (13), 4905–4910.
- COOK, K.D. 1986 Electrohydrodynamic mass-spectrometry. *Mass Spectrom. Rev.* **5** (4), 467–519.
- FEDKIW, T.P. & LOZANO, P.C. 2009 Development and characterization of an iodine field emission ion source for focused ion beam applications. *J. Vac. Sci. Technol. B* **27** (6), 2648–2653.
- FERNÁNDEZ DE LA MORA, J. 2007 The fluid dynamics of Taylor cones. *Annu. Rev. Fluid Mech.* **39** (1), 217–243.
- GABOVICH, M.D. 1983 Liquid-metal ion emitters. *Sov. Phys. Uspekhi* **26** (5), 447–455.
- GAMERO-CASTAÑO, M. 2008 Characterization of the electrospays of 1-ethyl-3-methylimidazolium Bis(Trifluoromethylsulfonyl) imide in vacuum. *Phys. Fluids* **20**, 032103.
- GAMERO-CASTAÑO, M. 2010 Energy dissipation in electrospays and the geometric scaling of the transition region of cone-jets. *J. Fluid Mech.* **662**, 493–513.
- GAMERO-CASTAÑO, M. 2019 Dissipation in cone-jet electrospays and departure from isothermal operation. *Phys. Rev. E* **99** (6), 1–5.
- GAMERO-CASTAÑO, M. & CISQUELLA-SERRA, A. 2021 Electrospays of highly conducting liquids: a study of droplet and ion emission based on retarding potential and time-of-flight spectrometry. *Phys. Rev. Fluids* **6** (1), 013701.
- GAMERO-CASTAÑO, M. & FERNÁNDEZ DE LA MORA, J. 2000 Direct measurement of Ion evaporation kinetics from electrified liquid surfaces. *J. Chem. Phys.* **113** (2), 815–832.
- GAMERO-CASTAÑO, M. & HRUBY, V. 2001 Electro spray as a source of nanoparticles for efficient colloid thrusters. *J. Propul. Power* **17** (5), 977–987.

- GAMERO-CASTAÑO, M. & HRUBY, V. 2002 Electric measurements of charged sprays emitted by cone-jets. *J. Fluid Mech.* **459**, 245–276.
- GAMERO-CASTAÑO, M. & MAGNANI, M. 2018 Numerical simulation of electro spraying in the cone-jet mode. *J. Fluid Mech.* **859**, 247–267.
- GAMERO-CASTAÑO, M. & MAGNANI, M. 2019 The minimum flow rate of electro sprays in the cone-jet mode. *J. Fluid Mech.* **876**, 553–572.
- GAÑÁN-CALVO, A.M. 1997 Cone-jet analytical extension of Taylor's electrostatic solution and the asymptotic universal scaling laws in electro spraying. *Phys. Rev. Lett.* **79**, 217–220.
- GAÑÁN-CALVO, A.M., LÓPEZ-HERRERA, J.M., HERRADA, M.A., RAMOS, A. & MONTANERO, J.M. 2018 Review on the physics of electro spray: from electrokinetics to the operating conditions of single and coaxial Taylor cone-jets, and AC electro spray. *J. Aerosol Sci.* **125**, 32–56.
- GUERRERO, I., BOCANEGRA, R., HIGUERA, F.J. & FERNANDEZ DE LA MORA, J. 2007 Ion evaporation from Taylor cones of propylene carbonate mixed with ionic liquids. *J. Fluid Mech.* **591**, 437–459.
- HIGUERA, F.J. 2003 Flow rate and electric current emitted by a Taylor cone. *J. Fluid Mech.* **484**, 303–327.
- IGNAT'EV, N.V., WELZ-BIERMANN, U., KUCHERYNA, A., BISSKY, G. & WILLNER, H. 2005 New ionic liquids with tris(perfluoroalkyl)trifluorophosphate (FAP) anions. *J. Fluorine Chem.* **126** (8), 1150–1159.
- KROHN, V. 1961 Liquid metal droplets for heavy particle propulsion. In *Electrostatic Propulsion*, pp. 73–80. American Institute of Aeronautics and Astronautics.
- LARRIBA, C., CASTRO, S., FERNANDEZ DE LA MORA, J. & LOZANO, P. 2007 Monoenergetic source of kilodalton ions from Taylor cones of ionic liquids. *J. Appl. Phys.* **101** (8), 1–6.
- LOZANO, P. & MARTINEZ-SANCHEZ, M. 2004 Ionic liquid ion sources: suppression of electrochemical reactions using voltage alternation. *J. Colloid Interface Sci.* **280** (1), 149–154.
- MILLER, C.E. & LOZANO, P.C. 2020 Measurement of the dissociation rates of ion clusters in ionic liquid ion sources. *Appl. Phys. Lett.* **116** (25), 3–8.
- PEREZ-LORENZO, L.J. & FERNANDEZ DE LA MORA, J. 2019 A new facility for electro spray propulsion studies with spatial resolution of the full beam and high-resolution mass analysis: remarks on drop versus ion propulsion. In *AFOSR Contractors Meeting Los Angeles, CA*.
- RICHARDSON, C.B., PIGG, A.L., & HIGHTOWER, R.L. 1989 On the stability limit of charged droplets. *Proc. R. Soc. Lond. A* **422**, 319–328.
- ROMERO-SANZ, I., BOCANEGRA, R., FERNÁNDEZ DE LA MORA, J., & GAMERO-CASTAÑO, M. 2003 Source of heavy molecular ions based on Taylor cones of ionic liquids operating in the pure ion evaporation regime. *J. Appl. Phys.* **94**(5), 3599–3605.
- SAFAROV, J., LESCH, F., SULEYMANLI, K., ALIYEV, A., SHAHVERDIYEV, A., HASSEL, E. & ABDULAGATOV, I. 2017 Viscosity, density, heat capacity, speed of sound and other derived properties of 1-butyl-3-methylimidazolium tris(pentafluoroethyl) trifluorophosphate over a wide range of temperature and at atmospheric pressure. *J. Chem. Engng Data* **62** (10), 3620–3631.
- SEKI, S., SERIZAWA, N., HAYAMIZU, K., TSUZUKI, S., UMEBAYASHI, Y., TAKEI, K. & MIYASHIRO, H. 2012 Physicochemical and electrochemical properties of 1-ethyl-3-methylimidazolium tris(pentafluoroethyl)trifluorophosphate and 1-ethyl-3-methylimidazolium tetracyanoborate. *J. Electrochem. Soc.* **159** (7), 967–971.
- SOUČKOVÁ, M., KLUMFAR, J. & PÁTEK, J. 2012 Temperature dependence of the surface tension and 0.1 MPa density for 1-C n-3-methylimidazolium tris(pentafluoroethyl)trifluorophosphate with n = 2, 4, and 6. *J. Chem. Thermodyn.* **48**, 267–275.
- TANG, K. & GOMEZ, A. 1994 On the structure of an electrostatic spray of monodisperse droplets. *Phys. Fluids* **6**, 2317.
- YANG, W., DUAN, H., LI, C. & DENG, W. 2014 Crossover of varicose and whipping instabilities in electrified microjets. *Phys. Rev. Lett.* **112**, 5.